
Article:
Prakash, A, Piazolo, S orcid.org/0000-0001-7723-8170, Saha, L et al. (3 more authors) (2018) Deformation behavior of migmatites: insights from microstructural analysis of a garnet–sillimanite–mullite–quartz–feldspar-bearing anatectic migmatite at Rampura–Agucha, Aravalli–Delhi Fold Belt, NW India. International Journal of Earth Sciences, 107 (6). pp. 2265-2292. ISSN 1437-3254

https://doi.org/10.1007/s00531-018-1598-6

Deformation behavior of migmatites: Insights from microstructural analysis of a garnet-sillimanite-mullite-quartz-feldspar bearing anatectic migmatite at Rampura-Agucha, Aravalli Delhi Fold Belt, NW India

Abhishek Prakash[1] · Sandra Piazolo [2,3] · Lopamudra Saha[1*] · Abhijit Bhattacharya[4] · Durgesh Kumar Pal[5] · Saheli Sarkar[1]

[1] Department of Earth Sciences, Indian Institute of Technology Roorkee, Roorkee-247667, India.

[2]GEMOC ARC National Key Centre and ARC Centre of Excellence Core to Crust Fluid Systems (CCFS), Department of Earth and Planetary Sciences Macquarie University, NSW 2109, Australia

[3]School of Earth and Environment, University of Leeds, Leeds. LS2 9JT, United Kingdom

[4]Department of Geology and Geophysics, Indian Institute of Technology Kharagpur, Kharagpur721302, India.

[5]AMETEK Instruments India Pvt., Ltd, Indian Institute of Technology (Indian School of Mines), Dhanbad, Dhanbad-826004, India.

[*]corresponding author email: saha.lopamudra@gmail.com

ABSTRACT

In the present study we investigate the microstructural development in mullite, quartz and garnet in an anatectic migmatite hosted within a Grenvillian-age shear zone in the Aravalli-Delhi Fold Belt. The migmatite exhibits three main deformation structures and fabrics (S_1, S_2, $S_{3)}$. Elongated garnet porphyroblasts are aligned parallel to the metatexite S_2 layers and contain crenulation hinges defined by biotite-sillimanite-mullite-quartz (with S_1 axial planar foliation). Microstructural evidence and phase equilibrium relations establish the garnet as a peritectic phase of incongruent melting by breakdown of biotite, sillimanite ± mullite and quartz at peak P-T of ~8 kbar, 730°C along a tight-loop, clockwise P-T path. Monazite dating establishes that the partial melting occurred between ~1000-870 Ma. The absence of subgrains and systematic crystal lattice distortions in these garnets despite their elongation suggest growth pseudomorphing preexisting 3-D networks of S_1 biotite aggregates rather than high temperature crystal plastic deformation which is noted in the S_1 quartz grains that exhibit strong crystallographic preferred orientation (CPO), undulatory extinction and subgrains. Mode-I fractures in these garnet porphyroblasts induced by high melt pressure during late stage of partial melt crystallization are filled by retrograde biotite-sillimanite. Weak CPO and non-systematic crystal lattice distortions in the coarse quartz grains within the S_2 leucosome domains indicate these crystallized during melt solidification without later crystal plastic deformation overprint. In the later stages of deformation (D_3), strain was mostly accommodated in the mullite-biotite-sillimanite rich restite domains that forming S_3 which warps around garnet and leucosome domains; consequently fine-grained S_3 quartz does not exhibit strong CPOs.

(252)

Keywords

Melt-present deformation; anatectic migmatites; crystal preferred orientation; quartz; garnet; rheology.

INTRODUCTION

Anatectic migmatites record signatures of partial melting events in mid- to deep-crustal levels at the roots of orogenic belts (Ashworth 1985; Brown 2001; Whitney et al. 2004; Beaumont et al. 2006). The restitic parts preserved in many migmatites are archives of the geological history that pre-dates the melting event (Guernina and Sawyer 2003; Sawyer 2008). Both experimental and theoretical work demonstrate that the dynamic viscosity of partially molten rocks is reduced by several orders of magnitude depending on the volume fraction of melt (Arzi 1978; Vigneresse et al. 1996; Berger and Kalt 1999; Takeda and Obata 2003). Therefore, in situations, where the production, segregation and emplacement of melts are synchronous with active deformation, strain is likely to be complexly partitioned into low-viscosity melt dominated layers within the deforming matrix of the bulk rock. However, in such experiments strain rates and temperatures are unrealistic thus experimental results may not be directly applied to study deformation patterns in migmatites (Paterson 1987; Rutter and Neumann 1995). Consequently, detailed studies of natural migmatites are crucial.

Deformation microstructures in minerals in anatectic migmatites in melt-dominated and melt-absent domains can be determined from quantitative orientation analysis including internal deformation features (e.g. subgrains) and their CPOs using electron backscatter diffraction (EBSD) studies (Venables and Harland 1973; Prior et al. 1999; Kleinschrodt and Duyester 2002; Ji et al. 2003; Mainprice et al. 2004; Storey and Prior 2005; Hasalová et al. 2008; Menegon et al. 2011; Cavalcante et al. 2013). The results of such EBSD studies may be combined with quantitative phase equilibrium modeling of melting reactions in migmatites to understand how naturally-occurring minerals respond to far-field stress before, at and after supra-solidus conditions. In this study, we integrate the results of phase equilibrium modelling

of anatectic migmatites using P–T pseudosection modelling and EBSD studies in a garnet-biotite-mullite migmatite of the Bhilwara Supergroup (Fig. 1a) from a Grenvillian-age, Northern Indian shear zone to demonstrate the complex interplay between deformation strain, mineralogical reactions and crystallization microstructures developed in quartz, mullite and garnet at subsolidus and supra-solidus condition.

GEOLOGICAL BACKGROUND AND FIELD RELATIONSHIPS

The chosen field area lies in the Bhilwara Supergroup of Northern India (Fig. 1a). The Bhilwara Supergroup rocks are exposed along the central and eastern parts of Aravalli-Delhi Fold Belt (Raja Rao 1976; Gupta et al. 1980; 1997, Fig. 1b). Two distinct NNE-SSW trending belts constitute the Bhilwara Supergroup: (i) the western Meso- to Neoproterozoic amphibolite facies schist belt that extends from Rajpura-Dariba in the south-west to Pur-Banera in the north-east and the (ii) eastern migmatite belt that extends up to the volcano-sedimentary successions of the Hindoli Group and Jahazpur Belt in the east, the granitoids and metasedimentary units of the North Delhi Fold Belt in the north (Fig. 1b; Gupta et al. 1997). The western schist belt consists of an interlayered sequence of garnet-staurolite-kyanite mica schists, calc-silicate gneisses and quartzites (Hazarika et al. 2013; Ojha et al. 2016). The garnet-sillimanite-biotite gneiss from which the sample studied stems forms the dominant lithology of the eastern anatectic migmatite belt and is associated with porphyritic granitoid plutons (Hazarika et al. 2013). The Archaean (~2.5 Ga) Berach granite (also called Banded Gneissic Complex, BGC-I; Heron 1953) and the ~Palaeoproterozoic greenschist facies metasedimentary units of the Aravalli Supergroup defines the southern margin of Bhilwara Supergroup. Along their western margin, the migmatites of Bhilwara Supergroup share a NNE trending tectonic contact (marked by ductile shear zones) with the polycyclic Meso- to Neoproterozoic granulites of the Mangalwar Complex and Sandmata Complex (together forming BGC-II, Heron 1953). Raja

Rao (1976) and Gupta et al. (1980, 1997) propose the BGC-I to represent the basement for the Bhilwara Supergroup.

Geochronological data from the Bhilwara Supergroup are sparse. A single zircon age of ~1.45 Ga is reported from the mylonitized porphyritic granitoid in Rampura-Agucha (Roy and Jhakar 2002). A Pb-Pb model age of ~1.8 Ga is obtained by Deb and Thorpe (2004) and Deb et al. (1989) for the anatectic metapelites in Rampura-Agucha. Based on U-Th-Pb (total) age determinations, Hazarika et al. (2013) obtained a single age population of ~1.0 Ga in monazites in the pelitic migmatites of the area. However, multiple monazite age populations have been obtained from the garnet-staurolite-kyanite mica schists of the Rajpura-Dariba interpreted to date peak and retrograde metamorphic events (1.87 and 1.62 Ga; Hazarika et al. 2013) and Pur-Banera (1.37 and 1.05 Ga; Ojha et al. 2016).

The field area at Rampura-Agucha lies close to the north-western margin of the migmatite belt (Fig. 1b). It is characterized by an ensemble of calc-silicate gneisses, amphibolites and anatectic garnet–biotite–sillimanite gneisses and mylonitized porphyritic granitoids (Fig. 1c). Three fabric-forming events are recognized in the garnet-biotite-sillimanite migmatites (Fig. 2a). We use a numbering system in accordance to relative age established in the field. The S_1 fabric is noted exclusively as inclusion trails within garnet porphyroblasts (Table 1; Fig. 3a). The first set of mesoscopic fabric (S_2) is defined by garnet-bearing leucosomes in a mesocratic matrix dominated by biotite intergrown with sillimanite, and coarse-grained quartz lenticles. The metatexite S_2 layers are co-axially refolded (hook-shaped fold superposition structures are common) by isoclinal D_3 folds and locally developed NNE-trending tight to open D_4 folds that plunge towards NNE (Fig. 2a). The axial planar fabric (S_3) is mutually indistinguishable from S_2, except at D_3 fold hinges (Figs 2b-c). In contrast, D_4 folding does not result in a recognizable fabric.

We selected a representative sample of the neosome part of the metatexite migmatite from a limb of a D_3 fold, with typical garnet bearing leucosome and restitic fine-grained layers warping around the leucosome layers (Figs 2b, c). No D_4 deformation features are seen at the sample location.

ANALYTICAL METHODS

Mineral chemistry and bulk chemistry

Mineral–chemical analyses of an anatectic garnet-biotite-sillimanite gneiss (RAM-1; Fig 2b, c) were carried out with a CAMECA SX (EPMA) at Indian School of Mines, Dhanbad. Operating conditions for feldspar analyses were acceteration voltage 15 kV with 15 nA beam current, and 15 kV, 20 nA were used for biotite, garnet, sillimanite and ilmenite. In built ZAF corrections were applied.

For pseudosection modeling, the bulk composition for the sample RAM-1 was determined by X-ray fluoresence at the National Geophysical Research Institute, Hyderabad. The analysis was done using a Phillips MagiX PRO Model 2440 XRF spectrometer.

Quantitative microstructural analysis and representation

Electron back-scatter diffraction (EBSD) analyses was done at Macquarie University on thin sections (sample RAM–1) cut perpendicular to S_2 foliation (Y-X plane) and parallel to the fold axis lineation of F_3 (X-direction). Thin sections were carbon coated (~3 nm thick) following mechano-chemical polishing using colloaidal silica. Full crystallographic orientation data were collected using automatically indexed EBSD patterns, acquired with an HKL Nordlys Nano high sensitivity EBSD detector and indexed using the Aztec analysis software (Oxford Instruments). The SEM was run at a high vacuum, with an accelerating voltage of 20kV, beam current of 8.2 nA, and with an aperture of 70 μm at a working distance of 9.5 -10.5 mm. Data was collected on rectangular grids with step size of 5-25 μm -(depending on the required spatial

154 resolution of the crystallographic information) using a beam scan. Noise reduction on the raw
155 data was performed following the procedure tested by Piazolo et al. (2006), Bestmann and
156 Prior (2003) and Prior et al. (2002). In pole figures, data is represented as one point per grain,
157 where a grain is defined as an area completely surrounded by high angle (>10°) boundaries.
158 Grains which have a mean internal misorientation <1° are considered to be strain free (Piazolo
159 et al. 2006).

160 **Monazite analyses**

161 Th-U-Pb (total) age determinations in monazites were computed from analytical data obtained
162 using the Cameca SX electron microprobe analyzer at the Indian School of Mines, Dhanbad
163 following the "age calibration" (Petrík and Konečný 2009). These age data are then corrected
164 against an age standard dated by SIMS method (Tomasck et al. 1998). Analytical settings were
165 set as follows: counting times for Pb 150 s, Th 45 s, U 75 s, Y 45 s, and for all other elements
166 25–35 s; sample current 100–130 nA; beam diameter ~3 μm. Standards used were the
167 following: P – Apatite, Ca – Wollastonite, La- La Glass, Ce- Ce Glass, Eu-Eu Glass, Si- Albite,
168 Y-YAG, Al- Kyanite, Pb- Crocoite, Th-Thorium Glass, U- Uranium Glass, Pr-Pr Glass, Nd-
169 Nd Glass, Sm- Sm Glass, Gd-Gd Glass, Dy -Dy Glass, Lu- Lu Glass. All errors are given as
170 2σ. Deconvolution histograms were calculated using Isoplot 4.15 (Ludwig 2001).

171 **RESULTS**

172 **General microstructure phase relationships and mineral chemistry**

173 S_2 foliation is defined by alternate melanocratic bands consisting of garnet porphyroblasts,
174 biotite (Bt_2), quartz (Qtz_2) and leucocratic bands consisting of quartz (Qtz_2), plagioclase (Pl_2),
175 potash feldspar (Kfs_2; Fig. 3a). Mineralogically similar leucocratic domains are also recognized
176 in the pressure shadows of the garnet porphyroblasts (Table 1; Fig. 3a). Garnet porphyroblasts
177 in the melanocratic bands of the penetrative S_2 metatexite layers are often elongated with aspect

ratios of 1.75 to 3.1 (Figs 3c, 4). Often bulbous and lobate coarse, strain free quartz (Qtz_2) grains are intergrown with garnets. Fractures within garnet porphyroblasts are oriented perpendicular to porphyroblast elongation (Table 1; Fig. 3c). These fractures in garnet are filled with biotite (Fig. 3c) or biotite-mullite-sillimanite (Fig. 3a). In garnet porphyroblasts D_1 crenulation hinges are mainly defined by mullite (Mul_1) and sillimanite (Sil_1) (Figs 3a, b, 4). Inclusion trails of quartz (Qtz_1) ribbons and resititic biotite (Bt_1) grains are axial planar to these crenulations. Qtz_1 from the relict D_1 hinges in the matrix exhibit undulose extinction and distinct subgrains (Figs 3h-i). Rootless crenulation hinges (defined by Bt_1+Sil_1+Mul_1), that formed during D_1 with orientation similar to those within garnet porphyroblasts also occur in the interfolial domains of S_3 (Fig. 3a). Coarse potash feldspar (Kfs_2) grains in the leucocratic layers of S_2 contain sillimanite (Sil_1), biotite (Bt_1) and quartz (Qtz_1) grains (Table 1; Figs 3d, e). Quartz (Qtz_1) inclusions in these potash feldspar (Kfs_2) grains are often rounded and form rims around biotite (Bt_1) inclusions (Fig. 3e). In leucocratic domains, plagioclase (Pl_2) with low dihedral angles occurs at the margins of coarse potash feldspar grains (Fig. 3f). The pervasive foliation in the sample is S_3 which is axial planar to the D_3 folds and transposes S_2. S_3 is defined by the shape-preferred aggregates of biotite (Bt_3), sillimanite (Sil_3) and mullite (Mul_3) that warp around garnet porphyroblasts in the melanocratic bands of S_2 (Figs 3a, b, 4 Table 1). In these S_3 domains, quartz is fine-grained. The interfolial domains of S_3 consist of the quartz-feldspar dominated S_2 leucosomes (Figs 3a, 4), with modally subordinate biotite, Bt_2 (Fig. 3a). To distinguish between the Bt+Sil+Mul assemblages in the S_3 foliation from those seen in garnet fractures, we label the latter as Bt_4+Sil_4+Mul_4 (Figs 3a, 3c, 3g).

X_{Mg} in the cores of garnet porphyroblasts are tightly constrained between 0.19 and 0.20 (Table 2). In contrast, the corresponding values at the rims of the garnet grains (~0.15-0.17) against S_3 biotite (Bt_3) and biotites in the fractures are variable, but against quartz grains, the values are identical. Biotite inclusions in garnet (Bt_1) and matrix biotite (Bt_2) in the S_2 foliation

show near-identical X_{Mg} (0.54 for one Bt_1 analyses and 0.55-0.56 for Bt_2) and TiO_2 contents (2.11 pfu for Bt_1 and 1.74-1.99 pfu for Bt_2; Table 2). X_{Mg} and TiO_2 values of coarse biotite grains (Bt_3) from the S_3 foliation range from 0.55-0.58 and 1.21-2.13 pfu, respectively. The X_{Mg} values of Bt_3 are similar to that of the Bt_1 and Bt_2, although their TiO_2 contents show significant variations. Biotites filling the fractures in garnets (Bt_4) are richer in Mg than Bt_1, Bt_2 and Bt_3. TiO_2 content of biotites in garnet fractures (Bt_4) is in the range 0.1-0.89 pfu (Table 2).

Mineral paragenetic relationships: Their interpretation in terms of succession of geological events

The succession of mineral assemblages that is stable with quartz and plagioclase is shown schematically in Figure 4. The warping of Bt_3+Sil_3+Mul_3 aggregates around garnet porphyroblasts and S_3 continuity indicates pre-D_3 garnet (Fig. 3a) growth and fracturing. Coarse K–feldspar (Kfs_2) grains in the leucosomes rimming the garnet porphyroblasts, and those occurring in S_3 interfolial domains, host biotite (Bt_1), sillimanite (Sil_1), and quartz (Qtz_1) inclusions, indicating K-feldspar and garnet crystallized from melt (Figs 3d-e). Bt_2 at the contacts of garnets with globular quartz (Qtz_2) grains and with the leucocratic layers of S_2 are also observed (Figs 3a, 3g). The occurrence of garnet within leucocratic domains indicate garnet formation was syn-D_2. Relict sillimanite (Sil_1)-mullite (Mul_1)–biotite (Bt_1) bearing crenulation hinges within garnet porphyroblasts, and in the S_3 interfolial domains indicates that these are D_1 deformation features overgrown by D_2 garnet porphyroblasts. The presence of thin films of plagioclase (Pl_2) around coarse K–feldspar (Kfs_2) and plagioclase ($Pl_{1/2}$) in the leucosome and the coarse quartz (Qtz_2) grains intergrown with garnet corroborate anatexis synchronous with D_2 (Figs 3e-f). Coarse quartz (Qtz_2) and plagioclase (Pl_2) within garnet grains in Fig. 3j are interpreted to have crystallised from trapped melt.

228 Bt_4+Sil_4+Mul_4 assemblages present in garnet fractures or Bt_4 at the contact with garnet
229 margins and at the contacts of garnet and Qtz_2 are interpreted to represent the retrograde
230 assemblage generated by back reactions of melt in garnet fractures and boundaries. Similar
231 TiO_2 content (1.77 pfu) noted in one such biotite grains (Table 2) with some of the biotite grains
232 (Bt_3; 1.74-1.88 pfu) from the S_3 layers indicate that they crystallized at comparable
233 temperatures. Hence we conclude that retrogression along garnet fractures is at the vaining
234 stages of D_2. The lower TiO_2 (0.1-0.59 pfu) and higher X_{Mg} (0.63-0.67) contents in most of the
235 biotite grains seen in garnet fractures compared to the Bt_3 suggest that biotite crystallization
236 continued to lower temperatures after the melt had largely crystallised and solid state
237 deformation occurred in S_3 fabric.

238 **Constraints on P-T conditions of melting**

239 A key factor in pseudosection analyses is to determine the 'effective bulk composition',
240 which represents the equilibration volume of the rock (Spear 1993; Stüwe 1997). This
241 equilibration volume varies from grain scale e.g. zoned minerals and reaction coronae
242 (Nasipuri et al., 2009) to larger scales, i.e. in hand specimen scale (Stuwe 2007; Kelsey et al.
243 2005, Nasipuri et al. 2009). In the studied migmatite sample RAM-1, garnet, biotite, and
244 plagioclase in different layers show strong compositional homogeneity (Table 2). This suggests
245 that the length scale of mineral equilibration attained during metamorphism was larger than the
246 scale of the layers of mineralogical segregations (Figs 2b-c); the equilibration was possibly
247 aided by element transfer across neosomes of varying width (couple of mm to cm) which are
248 seen to be commonly inter-layered and dispersed in biotire+sillimanite segregations.
249 Consequently, for pseudosection analyses we use the bulk rock composition derived from a
250 handspecimen to define the effective bulk composition (results given in Table 4).

251 P-T pseudosections were constructed (Table 4) in the NCKFMASH system using the
252 PERPLE_X (Connolly 2005) software built on the thermodynamic database of Holland and

Powell (1998,) modified in 2004. Manganese was excluded from the system as the spessartine contents in garnet is extremely low, and manganese is absent in other Fe-Mg phases (Table 2). The TiO_2 content in the rock is low and, therefore, also excluded in the computation. Solution models for phases used in P-T pseudosection modeling are: (i) garnet: hybrid model of Holland and Powell (1998), Engi and Wersin (1987); (ii) biotite: White et al. (2007), (iii) muscovite: hybrid model of Coggon and Holland (2002) and Auzanneau et al. (2010); (iv) feldspar: Benisek et al. (2004); (v) melt: hybrid model of Holland and Powell (2001) and White et al. (2001).

Melt volume percentages depend on the availability of free H_2O during initiation and progress of partial melting reactions (Webb et al. 2015). H_2O influencing partial melting reactions is primarily produced by dehydration reactions in surrounding rocks that may eventually get trapped in the rocks or added to the rock along shear zones (Brown 2002; White and Powell 2002; 2010; Webb et al. 2015). In order to estimate the H_2O available in the rock during partial melting under both H_2O–fluxed and H_2O–absent conditions, we constructed isobaric T–M_{H2O} pseudosections (Appendix 1a and b; M_{H2O} representing mol% of water in the bulk). We chose reference pressures of 6 and 8 kbar based on the 6-8 kbar pressure reported for the Grenvillian–age peak metamorphic condition obtained in mica schists of the Bhilwara Supergroup rocks from the Pu-Banera area (Ojha et al. 2016). The T-M_{H2O} pseudosections indicate stability of garnet-sillimanite–feldspar (ternary)–quartz–biotite–melt assemblage during H_2O–deficient melting at temperature ranges of 690-840°C, and during H_2O-fluxed melting at 690-750°C. H_2O contents for H_2O–undersaturated and water-fluxed conditions partial melting, as estimated from the T-M_{H2O} pseudosections have been considered for construction of the P-T pseudosections in Figs. 5a-d.

The P-T pseudosections show stability of the garnet–sillimanite–feldspar–quartz–biotite–melt peak metamorphic assemblage in P–T ranges of 5–8 kbar, 720–740°C during

H_2O–fluxed melting and ~780–850°C, 5–10 kbar at H_2O–absent melting (Figs 5a, 5e). In both cases, garnet modal isopleths increase with temperature and increasing melt modes and decreasing biotite and sillimanite modes thus indicating formation of garnet as a peritectic phase (Figs 5c-d). Within the field of the peak assemblage in the P-T pseudosections in Figs. 5b and 5f, (marked as yellow), the X_{Mg} isopleth of 0.2 for peritectic garnet (corresponding to the measured core composition of garnet porphyroblasts, table 2) is bracketed between 730°C and 780-800°C. The computed volume % of melt in equilibrium with garnet compositional isopleth of X_{Mg} = 0.2, in case of H_2O-fluxed melting is higher than the melt percolation threshold limit (~10-12 vol%) and lower for H_2O-absent melting (Figs 5d-e). Since the sample studied here is a migmatite where melt-rich layers form distinct bands supporting melt migration during formation of peritectic garnet porphyroblasts (Figs 2a-c), we propose that the partial melting for the rock occurred under H_2O-fluxed conditions when the mechanical conditions for melt segregation and migration was imparted. Peak pressure for stability of the assemblage garnet-biotite-sillimanite-melt is estimated to be ~8 kbar where the X_{Mg} isopleth (0.2) for garnet intersects the muscovite-in line (yellow field) in Figs. 5a-b (for water-fluxed melting). Based on isopleth thermometry from garnet composition, the peak P-T estimated is ~8 kbar, 730°C (Fig. 5b) for the following melting reaction (1):

Biotite (Bt_1) + sillimanite (Sil_1) + quartz (Qtz_1) + plagioclase + H_2O

→ garnet + melt (eqn. 1).

The reaction is also supported by the textural observations like occurrences of inclusion trails of biotite (Bt_1) and sillimanite (Sil_1) in garnet porphyroblasts (Figs 3a-b). The X_{An} isopleth of ~0.3 is the same as that measured in the plagioclase grains (in the leucocratic domains) in textural equilibrium with garnet. This isopleth intersects the garnet compositional isopleth of X_{Mg} =0.2 at the peak P-T conditions of ~8 kbar, 730°C (Fig. 5b). For conventional thermometry, we have chosen the near peak pressure of 8 kbar obtained from isopleths

thermobarometry as a reference pressure for calculating temperatures from garnet cores, rims and biotites (Bt_2) crystallized in melt rich domains. Average temperature obtained for these pairs is ~680°C (maximum and minimum values ranging from 670-690°C; Table 3). This temperature is within the temperature range obtained from the garnet core and biotite inclusion data (690°C). Any prograde path that may be proposed for reaction in equation 1 for the studied sample will cross the wet-solidus in the pseudosection, with increase in pressure and temperature (Fig. 5a).

Fractures in garnet porphyroblasts are filled with biotite and/or biotite + sillimanite + mullite (Figs 3a,c,g). High X_{Mg} values of biotites in these fractures indicate metamorphic origin rather than crystallization from any melt. So it is proposed that these biotites were formed by back reaction between melt trapped in fractures and garnets during melt-present reaction:

garnet + melt = biotite ± sillimanite ± mullite (eqn. 2).

Because of variable equilibration volumes for such reactions which are smaller than even a thin-section scale, their bulk composition cannot be determined and hence the reaction in equation 2 could not be modeled by any pseudosection analyses. Nevertheless, it may be predicted that the retrograde segment of any clockwise P-T path for such orogenic metamorphism will cross the H_2O-saturated solidus for was H_2O-rich, leading to the formation of the retrograde Bt_4±Sil_4±Mul_4 assemblage. For calculating the retrograde temperature range we have chosen the reference pressure at 6 kbar, which is the minimum pressure obtained for the retrograde section of P-T path in Fig. 10. At this reference pressure, rims of garnet against the adjoining biotites (Bt_3) in the S_3 fabric yield average temperature of ~570°C (maximum and minimum temperatures being 550-580°C, Table 3); this estimate is somewhat higher than the compositions of garnet and biotite (Bt_4) lodged in the garnet fracture (~540°C). biotite melting at ~6 kbar (Fig. 10). Hence, we infer that the retrograde section of the clockwise P-T path corroborates the back reaction between garnet and residual melt, which

Crystallographic and microstructural characterization

In order to constrain deformation mechanisms of the phases in presence of melt detailed crystallographic and microstructural analyses were carried out on garnet, quartz and mullite occurring within the different microstructural domains of the migmatite (Fig. 3a).

General orientation characteristics of mullite, quartz and garnet

Mullite: Mullite (Mul_1) occurring along the two limbs of D_1 micro folds hosted within D_2 garnet porphyroblasts shows contrasting orientations (Fig. 6a; b). Elongate mullite mats (Mul_3) defining the S_3 foliation in the matrix show a strong CPO, with the c-axes parallel to the stretching lineation (X-direction) and (010) plane perpendicular to the foliation plane (Figs 6c-d).

Quartz: Quartz occurs in different textural domains (Table 1, Fig. 4). Quartz grains at the hinges of D_1 rootless fold in the matrix (Qtz_1; Fig. 7a-b) exhibit a high number of subgrains and dauphine twins (60° rotation around c-axis) and a distinct CPO with clustering of (0001) poles to plane (Fig.7c). In contrast, quartz grains within leucocratic layers and intergrown with garnet (Qtz_2; Fig. 7b, 7d) show very weak to random CPO (Fig. 7e). The orientation map of the coarse quartz grains (Qtz_2) within S_2 leucosomes in the interfolial domains of S_3 is shown in Fig. 7f. Here, quartz grains exhibit lattice distortions, few continuous subgrain boundaries and a near random CPO (Fig. 7g). In contrast, a weak, but distinct CPO (Fig. 7i) is documented in fine-grained quartz (Qtz_3) in the biotite-mullite-sillimanite (Bt_3-Mul_3-Sil_3) dominated S_3 foliation (Figs 3a, 7h; 10).

Garnet: All analyzed garnet grains exhibit an elongate shape (e.g. Fig. 8a,b,d). All grains have very similar crystallographic orientations (Fig. 8e) even if these grains do not appear to be physically continuous in the plane of observation (Fig. 3a). The crystallographic orientation

map of a representative elongate garnet grain from the S_2 melanocratic band shows an absence of distinct subgrain boundaries and/or systematic crystal lattice bending. However, distinct changes in orientation are seen associated with fractures filled or not filled by quartz, biotite and mullite (Mul_3-Bt_3) (Fig. 8b,c,d). Analysis of other garnet grains show the same absence of systematic crystal lattice distortion or subgrain boundaries.

Monazite dating

Monazites in the sample occur as inclusions in garnet, quartz (Qtz_2) and potash feldspar (Kfs_2) in the S_2 layer, and overgrowing D_1 crenulation hinges (Figs 9a-d). Monazite grains are often anhedral and vary in size from 40-100μm (Figs 9c-o). BSE images show that the monazite grains are mostly homogeneous in composition with some grains having yitrium rich cores. Monazites included in garnet and potash feldspar (Kfs_2) yield 1028 Ma and 920-912 Ma respectively (Figs 9a,d,g,k). Cores of monazites occurring within S_2 melt bearing layer yield ages ranging from 1037-930 Ma and ages recorded from their rims vary from 887-840 Ma (Figs 9 e-f, h, n; Table 5). Monazites from the S_3 foliations yield 965-889 Ma from the cores and 887-850 Ma from their rims (Figs 9i, l-m, o; Table 5). The 33 monazite spot ages obtained from 15 grains yield two unmixed populations: 914±11 Ma and 1285±64 Ma (Fig. 9r). The older age population (~1285 Ma) is obtained from the core of one monazite included in a garnet porphyroblast.

DISCUSSION

Conditions of migmatisation and synchronous deformation

Field and microscopic observations indicate that melting in the garnet-sillimanite migmatites of Rampura-Agucha initiated post-D_1, and was pronounced during the D_2 deformation stage resulting in melt segregation and formation of S_2 layering including coarse-grained leucocratic, garnet-bearing bands and fine-grained, restititic layers dominated by biotite, mullite and some

quartz. The absence of melts cross-cutting D_3 fabrics precludes anatexis during or after the D_3 deformation.

Microstructural observations (Figs. 3a-b) and pseudosection analyses indicate that the D_2 peritectic garnet was formed during a H_2O-fluxed partial melting event at the expense of D_1 biotite-sillimanite aggregates at ~ 725°C and at pressure ~ 8 kbar under granulite facies conditions indicated by isopleth thermometry involving garnet compositions (Figs 5b, 10). The temperature recorded is thus close to the biotite melting reaction temperatures determined from pseudosection modeling using average metapelite bulk composition (White et al., 2001; Saha et al., 2008). A tight-loop clockwise P-T path constructed for the metamorphic event (Fig. 10), indicates rapid burial and exhumation. Since the garnet porphyroblasts are chemically homogeneous, it is suggested that high degree of chemical equilibrium was attained at the anatectic conditions as ubiqutous melt allowed rapid elemental exchange. Biotite and/or sillimanite in the fractures of garnet porphyroblasts were formed by back reactions with the melts trapped in the fractures during late stages of partial melt crystallization which marks the onset of retrogression (Figs. 3c; 10).

The Aravalli Delhi Fold Belt represents part of the Grenvillian–age orogeny in Northern India

Enclaves of polycyclic granulite facies migmatites from the Sandmata Complex of BGC-II (Fig. 1b) occur within charnockitic gneisses (Saha et al. 2008; Bhowmik et al. 2010). These migmatite enclaves record two partial melting events, namely M_1 at ~1.7-1.6 Ga in the sillimanite stability field, at 6-7 kbar and 850°C, followed by a second event (M_2) at ~1.0 Ga in kyanite stability field, at ~14 kbar, 850°C (Figs 5a, 5e; Saha et al. 2008). The high-pressure Grenvillian-age M_2 partial melting event recorded in the enclaves has also been recorded from the host felsic gneisses. Based on zircon and monazite ages from the gneisses of the Sandmata

Complex and Mangalwar Complex (Fig. 1b), Buick et al. (2006; 2010) proposed recycling of Paleo-Mesoproterozoic (~1.7-1.4 Ga) crustal components during the Grenvillian Delhi orogeny. Bhowmik et al. (2010) reported partial melting of gneisses from the Mangalwar Complex at ~12 kbar, 800°C during the Grenvillian orogeny (Figs 5a, 5e). In contrast, for the Grenvillian metamorphism from the Pur-Banera supracrustal sequence (Fig. 1b), Ojha et al. (2016) recorded peak P-T conditions of ~8 kbar, 600°C (Figs 5a, 5e).

In our sample, monazite aligned parallel to the S_2 and S_3 fabrics yield ages ranging between 1000-900 Ma (Fig. 9). Similar ages were also recorded by monazite grains sequestered within D_2 garnets suggesting an anataxis event at that time. Rims of monazites in the melt-rich layers yield spot ages of ~870-850 Ma, which may be interpreted as minimum age of melting and/or the age range of melt crystallization. Monazite yielding older ages of ~1286 Ma (Fig. 9) may be detrital.

In summary, the Rampura-Agucha metapelite migmatites underwent Grenvillian-age anatexis at ~8 kbar and 730°C. Peak P-T condition were thus at substantially lower pressures than those recorded westwards in the Sandmata Complex.

Evolution of deformation microstructures in the Rampura-Agucha migmatite: Characteristics and rheological implications

The correlation of microstructural development with the P-T path vector is given in Fig. 10. Contrasting orientations of mullite (Mul_1) grains in the limbs of the micro-folds hosted within garnet porphyroblast are consistent with systematic re-orientation (by rigid body rotation) of initially highly aligned mullite grains that inherited strong crystallographic preferred orientation during growth syn-tectonic with D_1 prior to melting. Solid state, prograde high strain is manifested by coarse quartz grains (Qtz_1) with undulose extinction and subgrains (Figs 3h-i). EBSD analyses of these quartz grains (Qtz_1) in the relict D_1 crenulation hinge in

428 the matrix show a distinct CPO (Figs 7a-c). The orientation of the c-axis relative to the
429 reference frame along with the presence of undulatory extinction and distinct subgrains with
430 continuous systematic subgrain boundaries suggests solid state deformation via dislocation
431 creep. The patterns observed in the pole figure is consistent with a dominance of <c> slip
432 suggesting high-T (650-700°C) deformation during D_1 (Blumenfild et al. 1986, Passchier and
433 Trouw 2005; Law 2012; Fig. 7b) .

434 Quartz grains in the leucocratic S_2 domains in the migmatite are coarser than 200µm
435 and exhibit a very weak to random CPO. Interestingly, despite near absence of a CPO,
436 internally the grains show weak undulatory extinction, and few, discontinuous subgrain
437 boundaries (Fig. 7f-g). We interpret these features to originate from the local stresses that occur
438 when a melt cools and quartz crystallizes and grows as one of the last phases. During this phase,
439 minor solid state crystal plastic deformation can be induced, resulting in the observed internal
440 deformation features, but since deformation is not due to regional differential stress, no distinct
441 CPO develops. Similar features have been described by Hasalova et al. (2011) in frozen-in
442 partial melts. We suggest that the newly crystallized coarse quartz grains escaped deformation
443 post-anatexis because as the melt pool solidified, strain was partitioned first into adjacent melt-
444 bearing rheologically weak domains; hence the solidified melt pool deformed only to a minor
445 extent. Once, all melt had solidified these coarse-grained domains were not subjected to the
446 significant solid state deformation. This lack of crystal plastic deformation imposed during
447 later retrograde deformation is similar to conclusions for similar migmatitic rocks (Hasalova et
448 al. 2011, Menegon et al. 2011).

449 In contrast, in the S_3 realms the polygonised, finer-grained quartz aggregate (10-50 µm;
450 Fig. 10; Fig. 7h) shows a weak CPO (Fig. 7i). These aggregates are interleaved with relict
451 prograde biotite, sillimanite and mullite layers that anastomose around the coarser-grained
452 domains. The relict nature of the latter phases is inferred from the chemistry of the biotites and

453 is therefore also interpreted to represent the restitic parts of a migmatite. Based on to the
454 geometric warping around the coarse-grained garnet bearing leucosome, these fine-grained,
455 phase mixed layers must have deformed post-migmatisation accommodating strain during the
456 retrograde path. We suggest that deformation occurred during solid state where most of the
457 strain was taken up by the basal slip of biotite along with rigid body rotation of biotite and
458 mullite. Quartz is mostly "passive" as the rheologically weaker biotite and mullite concentrate
459 strain. Therefore, quartz exhibits only minor internal lattice distortions and a weak CPO (Fig.
460 7i). We prefer this interpretation to the possibility of dislocation glide accommodated grain
461 boundary sliding at high temperature (>700°C), aided by small grain sizes and possibily melt
462 presence at grain boundaries (Schmid 1982; Behrmann and Mainprice 1987; Brodie and Rutter
463 2000; Song and Ree 2007; Killan et al. 2011; Svahnberg and Piazolo 2011). Our preference is
464 based on the fact, that biotite is known to be weak and in mixed, multiphase layers a weak CPO
465 is possible to develop in the "harder" mineral phase. This is due to pronounced strain partitition
466 between easily deformed phases e.g. graphite or biotite and a phase requiring higher critical
467 resolved shear stress for activation of slip systems e.g. ice or quartz (Cyprych et al. 2016).
468 Furthermore, microstructurally there are no indications for melt film presence during D_3
469 deformation. A consequence of our interpretation is that at the time of the last deformation
470 event, the rock was relatively weak, not due to presence of melt, but due to the presence of
471 fine-grained phase mixed layers that developed during the transient migmatistationn event.
472 These fine-grained, biotite, mullite rich, restite layers deform at relatively low stresses as
473 suggested by experiments (e.g. of an analogues system of ice and graphite; Cyprych et al.
474 2016), hence are weak.

475 In summary, we interpret that high-strain deformation prevailed postdating anatexis.
476 Strain was accommodated by solid state deformation (D_3) within the fine-grained quartz
477 aggregates interleaved with biotite aggregates forming rheologically weak layers, and not by

478 the coarse-grained leucosome domains similar to strain partitioning seen in other layered
479 metamorphic rocks (e.g. Smith et al. 2015).

480 Large elongate garnet porphyroblasts described here seem at first sight to be similar to
481 those noted by several researchers in metamorphic rocks formed under granulite facies to
482 eclogite facies conditions (Ji and Martignole 1994; Prior et al. 2000; Kleinschrodt and Mc Grew
483 2000; Ji et al. 2003; Mainprice et al. 2004; Storey and Prior 2005). These studies conclude that
484 under both subsolidus and suprasolidus conditions at different crustal depths coarse garnet
485 crystals may achieve their elongated shape due to crystal-plastic deformation manifested by
486 clear subgrain boundaries and systematic lattice bending. In contrast, the elongate garnet in our
487 sample is characterized by the absence of subgrain boundaries and/or crystal lattice bending
488 (Figs 8a-b). The occurrence of vermicular quartz intergrown with garnet (Fig. 3b), melt films
489 at feldspar–garnet interfacess (Figs 3e-f), and melt-bearing domains trapped within garnets
490 (Fig. 8d, Fig. 10), unmistakably point to the presence of melt during garnet growth.
491 Furthermore, small plagioclase grains with low dihedral angles possibly represent melt
492 pseudomorphs (Fig. 3j; e.g. Sawyer, 2001). Hence, garnet is peritectic growing in response to
493 incongruent melting of biotite-sillimanite aggregates. The extensional Mode-I fractures in the
494 elongate garnet porphyroblasts may have been induced by a combination of high fluid/melt
495 pressure exerted by partial melt crystallization (Abe and Urai 2012; Komoroczi et al. 2013,
496 Rimsa et al. 2007, Tretiakova et al. 2016) as well as tectonic forces (Abe and Urai 2012;
497 Komoroczi et al. 2013). Subsequent to garnet fracturing, growth of biotite and mullite (Bt_4-
498 Mul_4) along fractures and along garnet margins (Figs 3a, g) indicate that melt-rich domains
499 remained in contact with the garnet-bearing layers to promote their growth during cooling and
500 back-reaction. However, these domains remained shielded during subsequent solid-state
501 deformation as garnet and surrounding coarse-grained quartz and orthoclase remained rigid at
502 the D_3 event.

503 We attribute the elongate shape of garnet to its growth via partial melting (reaction 1)
504 pseudomorphing a pre-existing three–dimensional network of biotite-sillimanite/mullite
505 clusters. Such a biotite-sillimanite network intergrowth explains the uniform crystallographic
506 orientation of garnet as one large garnet grew within the three–dimensional network. We
507 however concede that the statistics for making the inference is low (number of grains exposed
508 at the surface of the thin section analyzed = 15).

509 Mullite stable in the S_3 foliation domains shows no substructure but strong CPOs (Figs
510 6c-d), indicating either rigid body rotation in presence of high shear stress under solid state
511 (see Piazolo and Jaconelli 2013) or possibly by epitaxial replacements of Kfs_2 in the presence
512 of differentital stress inducing oriented growth during the same late-stage solid-state
513 deformation.

514

515 **CONCLUSIONS**

516 Our analyses of microstructural development in the garnet-sillimanite-mullite-quartz-feldspar-
517 biotite migmatite in the high-grade Aravalli Delhi Fold Belt help to identify the suprasolidus
518 to subsolidus deformation mechanisms in a migmatite preserving signatures of its prograde,
519 peak and retrograde pressure-temperature-deformation path experienced by the migmatite. The
520 following conclusions can be drawn:

521 During the Grenvillian Delhi Orogeny (spanning from 1000 Ma-870 Ma), garnet-
522 biotite-sillimanite-mullite-quartz-feldspar bearing migmatite from the shear zone in the
523 Rampura-Agucha area of Aravalli Delhi Fold Belt underwent crustal anatexis at ~8-9 kbar,
524 730°C which is at much lower depth (~30 km) compared to the high pressure crustal anatexis
525 of the migmatites from the SC and MC (~14 kbar, >40 km) in the west (Fig. 1). Three main
526 stages of fabric development (S_1-S_3) occurred in the rock during the orogeny, where the S_2
527 metatexite layers were formed on its prograde path which underwent folding leading to

formation of biotite-sillimanite-mullite-quartz bearing axial planar foliations (S_3). During peak conditions, anatectic incongruent melting reaction involved breakdown of biotite, sillimanite and formation of garnet bearing peritectic assemblage along a tight loop clockwise P-T path. The preservation of sillimanite-mullite-biotite-quartz bearing inclusion trails in the Grenvillian age garnet porphyroblasts and strong CPOs, undulose extinction and subgrain boundaries in quartz grains in the relict crenulation hinges in matrix and within garnets imply that the rock was subjected to a pre-Grenvillian solid state, high-temperature deformation event (>650-700°C).

Peritectic garnet porphyroblasts are elongated with aspect ratios varying from 3.1-1.7 with Mode-I fractures perpendicular to the elongation. Presence of biotite-sillimanite-mullite in these fractures indicate their crystallisation during back reaction of garnet and trapped hydrous melt during cooling. Absence of subgrain boundaries and systematic crystal lattice bending in the garnet porphyroblasts indicate that their elongated nature is not a result of ductile deformation. We suggest that the garnet grains attained elongated shape as a result of their growth over a 3-D network of pre-existing (prograde) biotite-sillimanite-mullite foliations. Post garnet growth, extensional Mode-I fractures formed due to local high melt pressure during vaining stages of anataxis in combination with tectonic stresses. Microstructural analyses of garnet from the study hence imply that elongated shapes of peritectic garnets especially those crystallised in equilibrium with melts need not necessary be due to ductile, crystal-plastic deformation and that under such conditions garnets may exhibit brittle behaviour.

Near-random two weak CPOs of coarse-grained quartz in the matrix S_2 indicate that crystallisation of melt outlasted high temperature (>700°C) D_2 deformation in these areas. Post-migmatisation solid state deformation was instead accommodated in the fine-grained quartz rich domains interleaved with biotite, sillimanite, mullite in the S_3 layers. These layers represent restitic layers formed during partial melting. During post-migmatisation deformation

these phase mixed, fine-grained layers act as rheological weak zones as they deform mainly by basal slip in biotite and rigid body rotation of both biotite and mullite and minor dislocation creep in quartz

Our study suggests that the inferred rheological weakness of migmatites may outlast the actually melt-present time period, as biotite rich layers developed during partial melting facilitates late stage, solid state deformation with low rheological strength.

TABLE CAPTIONS

Table 1.Characteristics of deformation microstructures and mineral assemblages.

Table 2. Electron probe microanalaytical data and structural formulae of silicate phases in RAM-1.

Table 3. Results of geothermobarometry for analysed sample RAM-1.

Table 4. Bulk rock major element oxides (in wt %) in analysed sample RAM-1.

Table 5. Electron probe microanalaytical data and spot age ($\pm 2\sigma$) data in monazites in analysed sample RAM-1.

ACKNOWLEDGEMENTS

LS acknowledges Faculty Initiation Grant, IIT Roorkee for conducting field work and for the analytical costs. LS also acknowledges Dr. M. Satyanarayanan, NGRI, Hyderabad, India for XRF analyses and Ms. Jyothirmayee Palaparthi for compiling the figures. SP acknowledges the Australian Research Council through her Future Fellowship (FT1101100070) for financial support. The authors thank one anonymous reviewer and Kåre Kullerud for their constructive reviews and Prof. Dullo for helpful editorship.

FIGURE CAPTIONS

Figure 1. (a) Generalised tectonic map of India showing the Archean cratons and Proterozoic mobile belts. Abbreviations used are ADFB: Aravalli Delhi Fold Belt, AC: Aravalli Craton, BuC: Bundelkhand Craton, SC: Singhbhum Craton, BC: Bastar Craton, EDC: Eastern Dharwar Craton, WDC: Western Dharwar Craton, CITZ: Central Indian Tectonic Zone, CGC: Chotanagpur Gneissic Complex, SPGC: Shillong Plateau Gneissic Complex, EGMB: Eastern Ghats Mobile Belt, SIG: South Indian Granulite terrain, HOB: Himalayan Orogenic Belt, DV: DeccanVolcanics; 1: Mahandi Rift, 2: Godavari Rift, 3: Closepet Granite. Grey regions show the Grenvillian orogenic belt. The study area (ADFB) is shown in the box. (b) Map showing different lithological and tectonic components of Aravalli Craton and Aravalli Delhi Fold Belt (modified after Heron, 1953; Roy and Jhakar, 2002). GF: Grenvillian Font after Ojha et al. (2016). Box indicates location of the study area. (c) Geological map of Bhilwara Supergroup from Rampura-Agucha area (modified after Roy 2002). Boxes show locations from which detailed structural analyses have been conducted and location (Rampura-Agucha mine pit) from which sample RAM-1 has been collected.

Figure 2. (a) Field photograph of anatectic garnet-biotite-sillimanite gneiss showing different stages of deformation (for detailed description see text). (b, c) Photographs showing the neosome parts of anatectic garnet-biotite-sillimanite bearing migmatite (RAM-1). Mineral abbreviations in the figures and tables are after (Kretz 1983). See text for description of structural elements in the rock.

Figure 3. Optical microphotographs (a-b, d-f, h-k), SEM image (c) and BSE image (g) displaying textures from RAM-1. (a) Photograph showing D_1 crenulation hinges (defined by sillimanite and mullite) within garnet and pervasive S_3 (defined by biotite, sillimanite, mullite),

602 warping around garnet porphyroblast. Quartz-feldspar bearing melt layers (S_2) occur within the
603 interfolial domains of S_3. Relict rootless D_1 crenulation hinges occur in the interfolial domains
604 of S_3; yellow arrow heads point to fracture filled with biotite and sillimanite/mullite (b) Garnet
605 porphyroblast preserving D_1 crenulation hinges and quartz inclusion trails axial planar to the
606 crenulation. (c) An elongated garnet porphyroblast in contact with S_3. (d) A coarse potash
607 feldspar grain (at contact of S_3 biotites), containing rounded quartz inclusions and biotite
608 inclusions. (e) Quartzo-feldspathic layer at contact of garnet porphyroblast showing melt-
609 related microstructures like randomly oriented sillimanite and mullite and biotite grains in
610 coarse potash feldspar, globular inclusions of quartz in potash feldspar and thin melt film (now
611 represented by plagioclase) in between potash feldspar grains. (f) Thin films of plagioclase
612 along the margins of coarser plagioclase indicate sites of melt crystallization. (g) Intergrowth
613 of garnet with globular quartz grains indicate crystallization in presence of melt. (h and i)
614 Coarse quartz grains in the D_1 crenulation hinges are strained, show undulose extinction
615 (yellow arrow) and presence of subgrains (red arrows). (j) Presence of euhedral plagioclase
616 grain at the contact of coarse quartz grains crystallised from melt trapped melt in D_2 garnet.
617 Note presence of relict sillimanite.
618
619 Figure 4. Schematic sketch showing deformation microstructures, i.e. (a) D_1 deformation; (b)
620 D_2 deformation; (c) D_3 deformation.
621
622 Figure 5. Pseudosections in NCKFMASH system from bulk composition of RAM-1. Molar
623 proportions under H_2O-fluxed conditions are SiO_2:Al_2O_3:FeO:MgO:CaO:Na_2O:K_2O: H_2O =
624 48.33:9.63:5.22:8.48:1.15:1.15:2.90:23.14. (a) P-T pseudosection under H_2O-fluxed melting
625 condition, showing stability field of garnet-sillimanite-feldspar-biotite-quartz-melt bearing
626 assemblage noted in the sample, at P-T ranges of 5-8 kbar, 725-780°C. (b) Compositional

isopleths of garnet, biotite and feldspar in the P-T pseudosection of C and star sign indicates highest P-T for melting reaction. (c and d) Modal isopleths of different phases in the P-T pseudosection of (a). (e) P-T pseudosection under H_2O-absent melting condition. Oxide molar proportions of the bulk is SiO_2:Al_2O_3:FeO:MgO:CaO:Na_2O:K_2O:H_2O = 58.09:11.57:6.27:10.19:1.38:1.38:3.49:7.62. (f) Compositional isopleths of garnet, biotite and feldspar in the P-T pseudosection of (e). The yellow, grey and pink shaded fields respectively show stability of biotite±garnet, orthopyroxene and cordierite with melt. M_{MC}, M_{SC} and M_{PB} show peak P-T conditions for the Grenvillian anatexis in the Mangalwar Complex (after Bhowmik et al. 2010), Sandmata Complex (after Saha et al. 2008) and Pur-Banera supracrustals (after Ojha et al 2016).

Figure 6. Orientation characteristics of different mullite types (a) Mul_1; orientation map of garnet grain (lilac) and mullite as inclusions in the grain; note hinge trace (dashed white lines); (b) 3D representation of mullite crystal orientation grains present as inclusion in garnet forming crenulation hinges shown in (a). (c) Orientation map of mullite Mul_3 intergrown with fine-grained biotite (khaki) and fine-grained quartz (red), for mullite colouring signifies crystal orientations as shown in inset. (d) Pole figures showing the orientation of Mul_3 mullite grains shown in (c); one point per grain.

Figure 7. Orientation characteristics of different quartz types. (a) Petrographic image of microfold made up by Qtz_1. (b) Orientation map of microfold limb shown in (a). (c) Pole figures of Qtz_1 corresponding to orientation map of microfold shown in (a,b). (d) Orientation map of Qtz_2 (quartz intergrwon with garnet porphyroblast); note presence of Dauphine twins (red lines) but absence of subgrain boundaries (yellow lines). (e) Pole figures and contour maps of quartz corresponding to orientation map (d). (f) Orientation map of Qtz_2 coarse-grained quartz

652 from the leucocratic layers of S_2. (g) Pole figures and contour maps of coarse-grained quartz
653 corresponding to orientation map (f). (h) Orientation map of fine-grained quartz, Qtz_3
654 intergrown with mullite (Mul_3) in the S_3 foliation planes. (i) Pole figures and contour maps of
655 fine-grained quartz corresponding to orientation map (h).

656 Figure 8. Orientation characteristics of garnet grains. (a) Map of elongate garnet grain with
657 surrounding minerals; different phases are shown in different colours; (b) Map of orientation
658 variations within garnet grain shown in (a), colour variations indicate the progressive internal
659 misorientation 0-2°. p-p' outline misorientation profile shown in (c); note in (a) and (b) location
660 of fractures is shown as stippled lines (c) Misorientation profile within grain along line p-p'
661 shown in (b). (d) photomicrograph of fracture within elongate garnet porphyroblast; (e) Pole
662 figures showing the orientation of all garnet grains by plotting data from 15 different garnet
663 grains; note the similarity in orientation.
664

665 Figure 9. Mcirostructural relations (BSE images) of the monazites (a-d), BSE images of the
666 monazite grains with spot ages (e-o), X-Ray Th and Y images of the monazite grain in o (p-q)
667 and probability density plot of monazite grains from the analysed sample RAM-1.
668

669 Figure 10. Summary of the P-T path inferred for the migmatite of Bilwara Supergroup from
670 the study area. Also shown are the calculated wet solidus (WSS) from Figure 5a, granite wet
671 solidus (GWS), granite dry solidus (GDS) curves (after Brown, 2002). Shematic drawings
672 show typical microstructures developed at the different segments of P-T path. Labeling of
673 deformation D_1 to D_3 according to discussion in text, in italic deformation mechanisms for
674 noted minerals. Thin section photograph shows presence of polygonal fine-grained quartz from
675 S_3 layers (marked with the box). See text for details. Abbreviations used for metamorphic facies

fields are: BS: blueschist, AmEc: amphibole eclogite, EpAm: epidote amphibole, GrtAm: garnet amphibolite, Gr: granulite.

Appendix-1. (a) and (b) T-M_{H2O} pseudosections at 6 kbar and 8 kbar respectively, showing stability fields of different minerals under water-deficient and water-fluxed conditions. High modal percentages of melt are observed in garnet-sillimanite-bioite- feldspar-quartz-melt bearing fields. Bulk compositions for C_0 and C_1 (in molar proportions) are respectively SiO_2: Al_2O_3: FeO: MgO: CaO: Na_2O: K_2O: H_2O = 62.68: 12.56: 6.77: 10.99: 1.49: 1.49: 3.77: 0.26 and 41.18: 8.25: 4.45: 7.22: 0.98: 0.98: 2.47: 34.46.

REFERENCES

Abe S, Urai JL (2012) Discrete element modelling of boudinage: Insights on rock rheology, matrix flow, and evolution of geometry. J Geophys Res 117:B01407.

Arzi AA (1978) Critical phenomena in the rheology of partially molten rocks. Tectonophysics 74:173-184

Ashworth JR (1985) Migmatites (Ashworth Ed.) Blackie, Glasgow

Auzanneau E, Schmidt MW, Vielzeuf D, Connolly JAD (2010) Titanium in phengite: a geobarometer for high temperature eclogites. Contrib Mineral Petr 159:1-24

Beaumont C, Nguyen MH, Jamieson RA, Ellis S (2006) Crustal flow modes in large hot orogens, in Channel Flow, Ductile Extrusion and Exhumation in Continental Collision Zones, edited by R. D. Law et al. Geological Society of London Special Publication 268:91–145

Behrmann J, Mainprice D (1987) Deformation mechanisms in a high-temperature quartz feldspar mylonite evidence for superplastic flow in the lower continental-crust. Tectonophysics 140:297-305

Benisek A, Kroll H, Cemic L (2004) New developments in two-feldspar thermometry. Am Mineral 89:1496-1504

Berger A, Kalt A (1999) Structures and Melt Fractions as Indicators of Rheology in Cordierite-Bearing Migmatites of the Bayerische Wald (Variscan Belt, Germany). J Petrol 40:1699-1719

715 Bestmann M, Prior DJ (2003) Intragranular dynamic recrystallization in naturally deformed
716 calcite marble: diffusion accommodated grain boundary sliding as a result of subgrain
717 rotation recrystallization. J Struct Geol 25:1597-1613
718
719 Bhattacharya A, Mohanty L, Maji A, Sen SK, Raith M (1992) Non-ideal mixing in the
720 phlogopite-annite boundary: Constraints from experimental data on Mg-Fe partitioning and
721 a reformulation of the biotite-garnet geothermometer. Contrib Mineral Petr 111:87–93
722
723 Bhowmik SK, Bernhardt HJ, Dasgupta S (2010) Grenvillian age high-pressure upper
724 amphibolite–granulite metamorphism in the Aravalli–Delhi Mobile Belt, North-western
725 India: new evidence from monazite chemical age and its implication. Precambrian Res
726 178:168–184
727
728 Blumenfeld P, Mainprice D, Bouchez JL (1986) C-slip in quartz from subsolidus deformed
729 granite. Tectonophysics 127:97-115
730
731 Brodie KH, Rutter EH (2000) Deformation mechanisms and rheology: why marble is
732 weaker than quartzite. Journal of Geological Society of London 157:1093–1096

733 Brown M (2001) Orogeny, migmatites and leucogranites: A review. Proc Indian Academy
734 of Science (Earth Planetary Sciences) 110:313-336

735 Brown M (2002) Retrograde processes in migmatites and granulites revisited. J Metamorph
736 Geol 20:25-40

737 Buick IS, Allen C, Pandit M, Rubatto D, Hermann J (2006) The Proterozoic magmatic and
738 metamorphic history of the Banded Gneiss Complex, central Rajasthan, India: LA-ICP-MS
739 U–Pb zircon constraints. Precambrian Res 151:119–142

740 Buick IS, Clark C, Rubatto D, Hermann J, Pandit MK, Hand M (2010) Constraints on the
741 Proterozoic evolution of the Aravalli–Delhi Orogenic belt (NW India) from monazite
742 geochronology and mineral trace element geochemistry. Lithos 120:511–528

743 Cavalcante GCG, Egydio-Silva M, Vauchez A, Camps P, Oliveira E (2013) Strain
744 distribution across a partially molten middle crust: Insights from the AMS mapping of the
745 Carlos Chagas Anatexite, Araçuaí belt (East Brazil). J Struct Geol 55:79-100
746
747 Coggon, R, Holland, TJB (2002) Mixing properties of phengitic micas and revised garnet-
748 phengite thermobarometers. J Metamorph Geol 20: 683-696
749
750 Connolly JAD (2005) Computation of phase equilibria by linear programming: a tool for
751 geodynamic modeling and its application to subduction zone decarbonation. Earth Planet
752 Sc Lett 236:524-541
753
754 Cyprych D, Piazolo S, Wilson CJ, Luzin V, Prior DJ (2016) Rheology, microstructure and
755 crystallographic preferred orientation of matrix containing a dispersed second phase:
756 Insight from experimentally deformed ice. Earth Planet Sc Lett, 449:272-281
757
758 Dasgupta S, Sengupta P, Guha D, Fukuoka M (1991) A refined garnet-biotite Fe-Mg
759 exchange geothermometer and its application in amphibolites and granulites. Contrib
760 Mineral Petr 109:130–137

761 Deb M, Thorpe RI, Cumming GL, Wagner PA (1989) Age, source and Strati-graphic
762 implications of Pb isotope data for conformable, sediment-hosted, base-metal deposits in
763 the Proterozoic Aravalli–Delhi Orogenic Belt, Northwestern India. Precambrian Res 43:1–
764 22

765 Engi M, Wersin X (1987) Something to do with grandite garnet. SMPM

766 Ferry JM, Spear FS (1978) Experimental calibration of the partitioning of Fe and Mg
767 between biotite and garnet. Contrib Mineral Petr 66:113–117

768 Gupta P, Mathur YK, Iqbaluddin, Prashad B, Sahai TN, Sharma SB (1997)
769 Lithostratigraphic map of the Aravalli region, southern Rajasthan and northeastern
770 Gujarat. Geological Survey of India Publications, Jaipur

771 Gupta SN, Arora YK, Mathur RK, Iqballuddin, Prasad B, Sahai TN, Sharma SB (1980)
772 Lithostratigraphic Map of the Aravalli Region. Scale 1:100,000. Geological Survey of
773 India, Calcutta
774
775 Guernina S, Sawyer EW (2003) Large-scale melt-depletion in granulite terranes: an
776 example from the Archean Ashuanipi Subprovince of Quebec. J Metamorph Geol 21:181-
777 201

778 Hasalová P, Schulmann K, Lexa O, Štípská P, Hrouda F, Ulrich S, Haloda J, Týcová P
779 (2008) Origin of migmatites by deformation-enhanced melt infiltration of orthogneiss: a
780 new model based on quantitative microstructural analysis. J Metamorph Geol 26:29-53
781
782 Hasalová P, Weinberg RF, Macre C (2011) Microstructural evidence for magma
783 confluence and reusage of magma pathways: implications for magma hybridization,
784 Karakoram Shear Zone in NW India. J Metamorph Geol 29:875-900
785
786 Hazarika P, Upadhyay D, Mishra B (2013) Contrasting geochronological evolution of the
787 Rajpura–Dariba and Rampura–Agucha metamorphosed Zn–Pb deposit, Aravalli–Delhi
788 Belt, India. J Asian Earth Sci 73:429-439

789 Heron AM (1953) Geology of central Rajasthan. Memoirs of the Geological Survey of
790 India 79: 339 p.
791
792 Holdaway MJ (2000) Application of new experimental and garnet Margules data to the
793 garnet–biotite geothermometer. Am Mineral 85:881–892

794 Holland TJB, Powell R (1998) An internally consistent thermodynamic data set for phases
795 of petrological interest. J Metamorph Geol 16:309-343

796 Holland T, Powell R (2001) Calculation of phase relations involving haplogranitic melts
797 using an internally consistent thermodynamic dataset. J Petrol 42:673-683

798 Ji SC, Martignole J (1994) Ductility of garnet as an indicator of extremely high-temperature
799 deformation. J Struct Geol 16:985–996
800

Ji SC, Saruwatari K, Mainprice D, Wirth R, Xu Z, Xia B (2003) Microstructures, petrofabrics and seismic properties of ultra high-pressure eclogites from Sulu region, China: implications for rheology of subducted continental crust and origin of mantle reflections. Tectonophysics 370:49–76

Kelsey D, White R, Powell R (2005) Calculated phase equilibria in K_2O-FeO-MgO-Al_2O_3-SiO_2-H_2O for silica-undersaturated sapphirine-bearing mineral assemblages. J Metamorph Geol 23:217-239

Kilian R, Heilbronner R, Stünitz H (2011) Quartz grain size reduction in a granitoid rock and the transition from dislocation to diffusion creep. J Struct Geol 33:1265-1284

Kleinschrodt R, McGrew A (2000) Garnet plasticity in the lower continental crust: implications for deformation mechanisms based on microstructures and SEM-electron channeling pattern analysis. J Struct Geol 22:795–809

Kleinshrodt R, Duyster JP (2002) HT-deformation of garnet: an EBSD study on granulites from Sri Lanka, India and the Ivrea Zone. J Struct Geol 24:1829-1844

Komoróczi A, Abe S, Urai JL (2013) Meshless numerical modeling of brittle–viscous deformation: first results on boudinage and hydrofracturing using a coupling of discrete element method (DEM) and smoothed particle hydrodynamics (SPH). Computational Geosciences 17:373-390

Ludwig KR (2001) User manual for Isoplot/Ex ver. 2.49: A geochronological toolkit for Microsoft Excel. Berkeley Geochronological Centre Special Publications 1a:1–56

Mainprice D, Bascou J, Cordier P, Tommasi A (2004) Crystal preferred orientations of garnet: comparison between numerical simulations and electron back-scattered diffraction (EBSD) measurements in naturally deformed eclogites. J Struct Geol 26:2089–2102

Menegon L, Nasipuri P, Stünitz H, Behrens H, Ravna E (2011) Dry and strong quartz during deformation of the lower crust in the presence of melt. J Geophys Res 116:B10410

Nasipuri P, Bhattacharya A, Das S (2009) Metamorphic reactions in dry and aluminous granulites: a Perple_X P–T pseudosection analysis of the influence of effective reaction volume. Contrib Mineral Petr 157:301–311

Passchier, CW, Trouw, RAJ (2005) Microtectonics. Springer-Verlag Berlin Heidelberg 366 pp.

Ojha MK, Mishra B, Hazarika P, Jeyagopal AV, Yadav GS (2016) EPMA monazite geochronology of the basement and supracrustal rocks within the Pur-Banera basin, Rajasthan: Evidence of Columbia breakup in Northwestern India. J Asian Earth Sci 117:284-303

839 Paterson MS (1987) Problems in the extrapolation of laboratory rheological
840 data.Tectonophysics 133:33-43

841 Petrìk I, Konečný P (2009) Metasomatic replacement of inherited metamorphic monazite
842 in a biotite-garnet granite from the NízkeTatry Mountains, Western Carpathians, Slovakia:
843 Chemical dating and evidence for disequilibrium melting. Am Mineral 94:957–74

844 Piazolo S, Bestmann M, Spiers C, Prior DJ (2006) Temperature dependent grain boundary
845 migration mechanisms: insights from insitu experiments. Tectonophysics 427:55–71

846 Piazolo S, Jaconelli P (2013) Sillimanite deformation mechanisms within a Grt-Sil-Bt
847 gneiss: effect of pre-deformation grain orientations and characteristics on mechanism, slip-
848 system activation and rheology. Geological Society London Special Publications 394:189-
849 213

850 Prior DJ, Boyle AP, Brenker F, Cheadle MC, Day A, Lopez G, Peruzzo L, Potts GJ, Reddy
851 S, Spiess R, Timms NE, Trimby P, Wheeler J, Zetterstrom L (1999) The application of
852 electron backscatter diffraction and orientation contrast imaging in the SEM to textural
853 problems in rocks. Am Mineral 84:1741-1759

854 Prior DJ, Wheeler J, Brenker FE, Harte B, Matthews M (2000) Crystal plasticity of natural
855 garnet: new microstructural evidence. Geology, 28:1003–1006
856

857 Prior DJ, Wheeler J, Peruzzo L, Spiess R, Storey C (2002) Some garnet microstructures:
858 an illustration of the potential of orientation maps and misorientation analysis in
859 microstructural studies. J Struct Geol 24:999–1011

860 Raja Rao CS (1976) Precambrian sequences of Rajasthan. Miscellaneous Publication of the
861 Geological Survey of India, 23, 497–516

862 Rimsa A, Whitehouse MJ, Piazolo S (2007) Brittle fracturing and fracture healing of zircon:
863 integrated cathodoluminescence, U-Th-Pb and REE study. Am Mineral 92:1213-1224
864

865 Roy AB, Jakhar SR (2002) Geology of Rajasthan (Northwest India) Precambrian to Recent.
866 Scientific Publishers, Jodhpur.

867 Rutter E, Neumann DHK (1995) Experimental deformation of partially molten Westerly
868 granite under fluid absent conditions, with implications for the extraction of granitic
869 magmas. J Geophys Res 100:15697-15715

870 Saha L, Bhowmik SK, Fukuoka M, Dasgupta S (2008) Contrasting episodes of regional
871 granulite facies metamorphism in enclaves and host gneisses from the Aravalli-Delhi
872 Mobile Belt, NW India. J Petrol 49:107–128
873

874 Sawyer EW (2001) Melt segregation in the continental crust: distribution and movement of
875 melt in anatectic rocks. J Metamorph Geol 19:291-309
876

Sawyer EW (2008) Atlas of migmatites. Mineralogical Associations of Canada Special Publication, 9

Schmid S (1982) Microfabric studies as indicators of deformation mechanisms and Microfabric studies as indicators of deformation mechanisms and flow laws operative in mountain building. In: Hsu, K. (Ed.), Mountain Building Processes. Academic Press, London, 95-110

Song WJ, Ree JH (2007) Effect of mica on the grain size of dynamically recrystallized quartz in a quartz-muscovite mylonite. J Struct Geol 29:1872-1881

Spear FS (1993) Metamorphic phase equilibria and pressure-temperature-time paths. Mineralogical Society America Monograph, Book Crafters, Chelsea, Michigan, USA

Storey CD, Prior DJ (2005) Plastic Deformation and Recrystallization of Garnet: A Mechanism to Facilitate Diffusion Creep. J Petrol 46:2593-2613

Stüwe K (1997) Effective bulk composition change due to cooling: a model predicting complexities in retrograde reaction textures. Contrib Mineral Petr 129:43–52

Stüwe, K., 2007. Geodynamics of the Lithosphere: Quantitative Description of Geological Problems, 2nd edition. Springer-Verlag, Berlin, Heidelberg, Dordrecht, p. 493.

Svahnberg H, Piazolo S (2010) The initiation of strain localisation in plagioclase-rich rocks: Insights from detailed microstructural analyses. J Struct Geol 32:1404-1416

Takeda Y–T, Obata M (2003) Some comments on the rheologically critical melt percentage. J Struct Geol, 25:813–818

Tomascak PB, Krogstad EJ, Walker RJ (1998) Sm-Nd isotope systematics and the derivation of granitic pegmatites in southwestern Maines. The Canadian Mineralogist 36:327-337

Tretiakova IG, Belousova EA, Malkovets VG, Griffin WL, Piazolo S, Pearson NJ, O'Reilly SW, Nishido H (2016) Recurrent magmatic activity on a lithosphere-scale structure: Crystallization and deformation in kimberlitic zircons. Gondwana Res 42:126-132

Venables JA, Harland CJ (1973) Electron back-scattering patterns--a new technique for obtaining crystallographic information in the SEM. Philosophical Magazine 27:1193-1200

Vigneresse JL, Barbey P, Cuney M (1996) Rheological transitions during partial melting and crystallization with application to felsic magma segregation and transfer. J Petrol 37:1579–1600

915 Webb G, Powell R, McLaren S (2015) Phase equilibria constraints on the melt fertility of
916 crustal rocks: the effect of subsolidus water loss. J Metamorph Geol, 33:147-165

917 White RW, Powell R, Holland TJB (2001) Calculation of partial melting equilibria in the
918 system Na_2O-CaO-K_2O-FeO-MgO-Al_2O_3-SiO_2-H_2O (NCKFMASH). J Metamorph Geol,
919 19:139-153

920 White RW, Powell R (2002) Melt loss and the preservation of granulite facies mineral
921 assemblages. J Metamorph Geol 20:621,632

922 White RW, Powell R, Holland TJB (2007) Progress relating to calculations of partial
923 melting equilibria for Metapelites. J Metamorph Geol 25:511–527
924

925 White RW, Powell R (2010) Retrograde melt-residue interaction and the formation of near-
926 anhydrous leucosomes in migmatites. J Metamorph Geol 28:579-597

927

928 Whitney D, Teyssier C, Vanderhaeghe O (2004) Gneiss Domes and Crustal Flow. In:
929 Geological Society of America Special Papers 380:15-330:15-33

Figure 1A-B

Click here to download Figure Figure 1A-B.eps

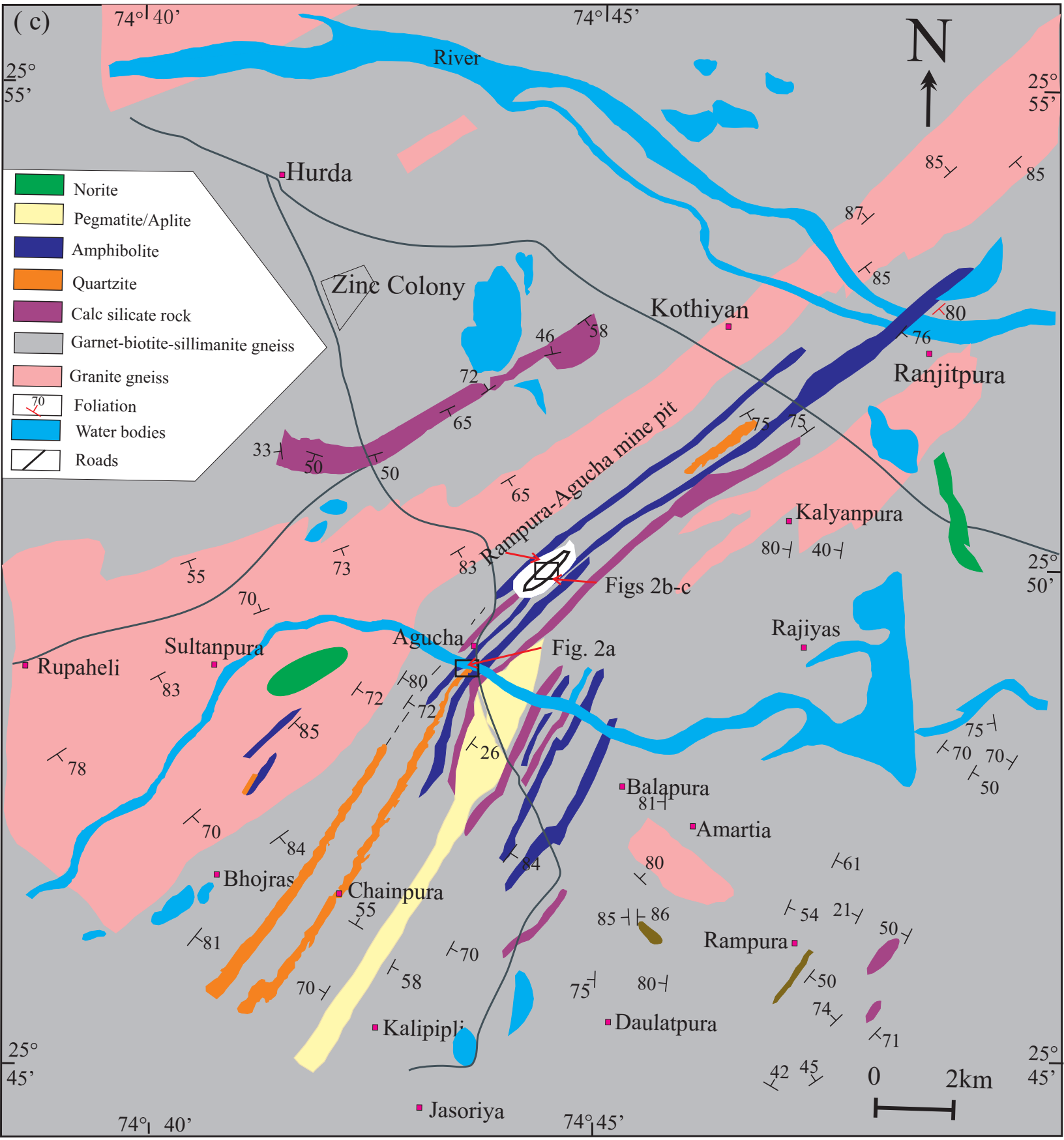

Figure 1

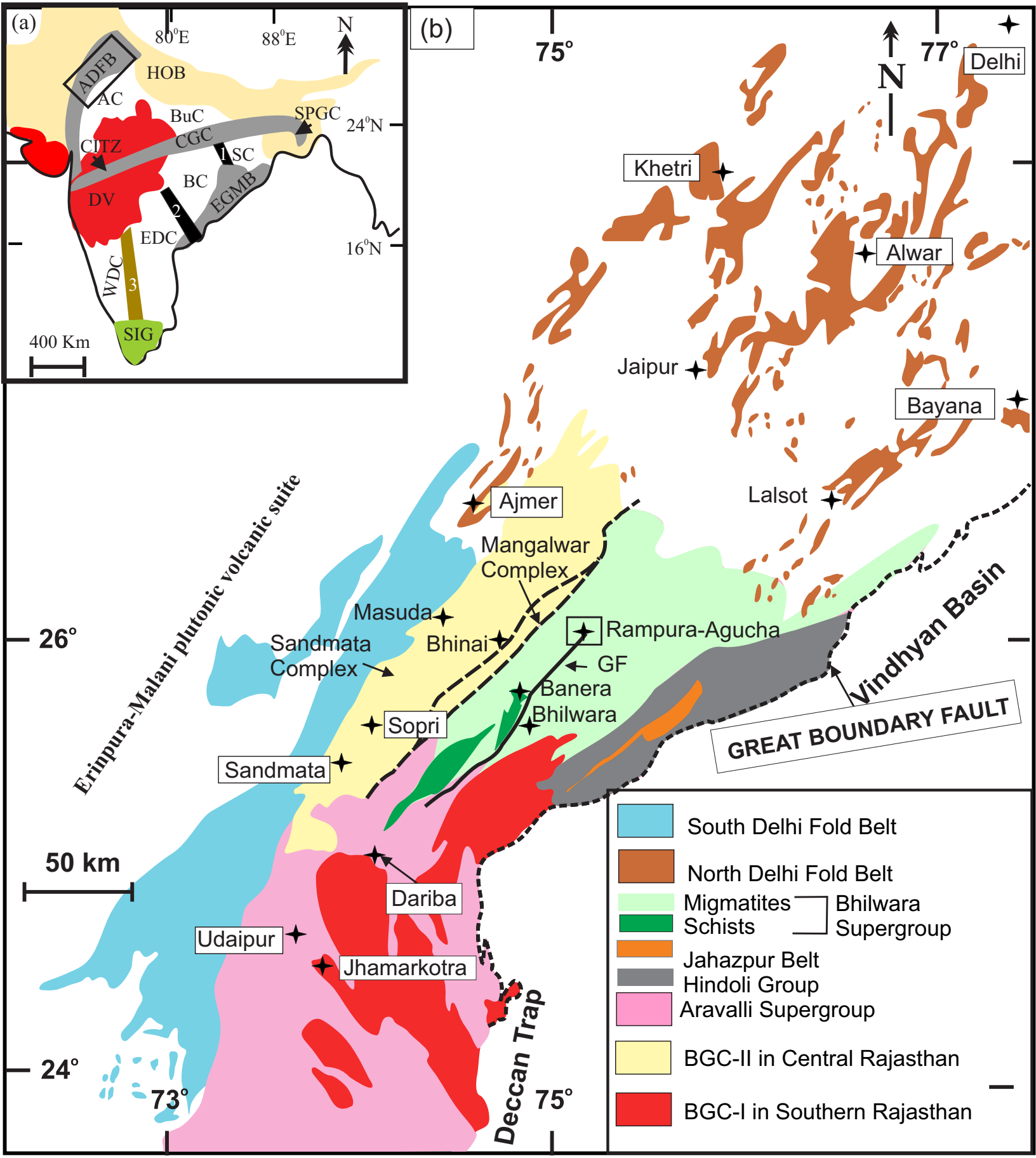

Figure 1

Figure 2

Click here to download Figure Figure 2.eps

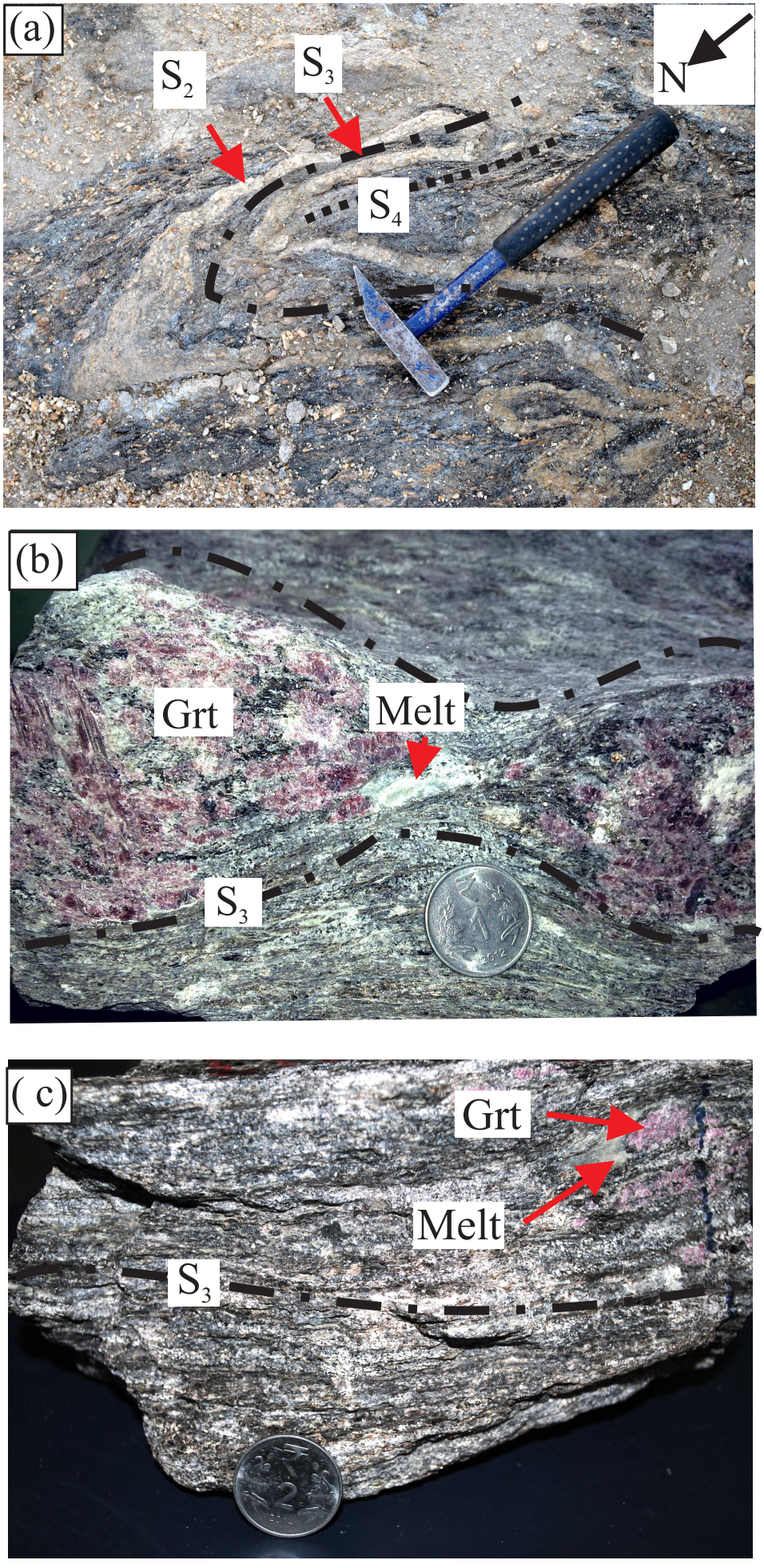

Figure 2

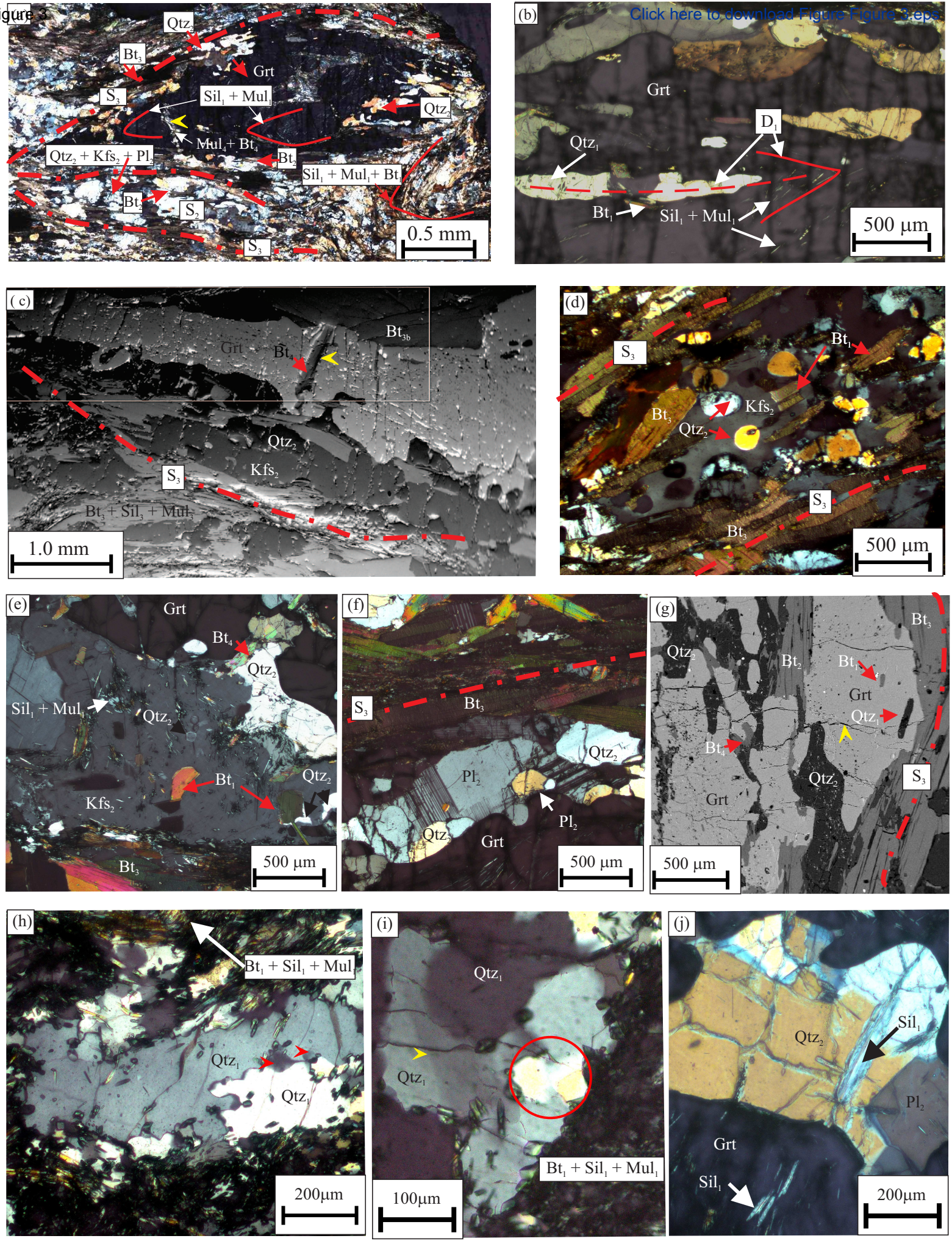

Figure 3

Figure 4

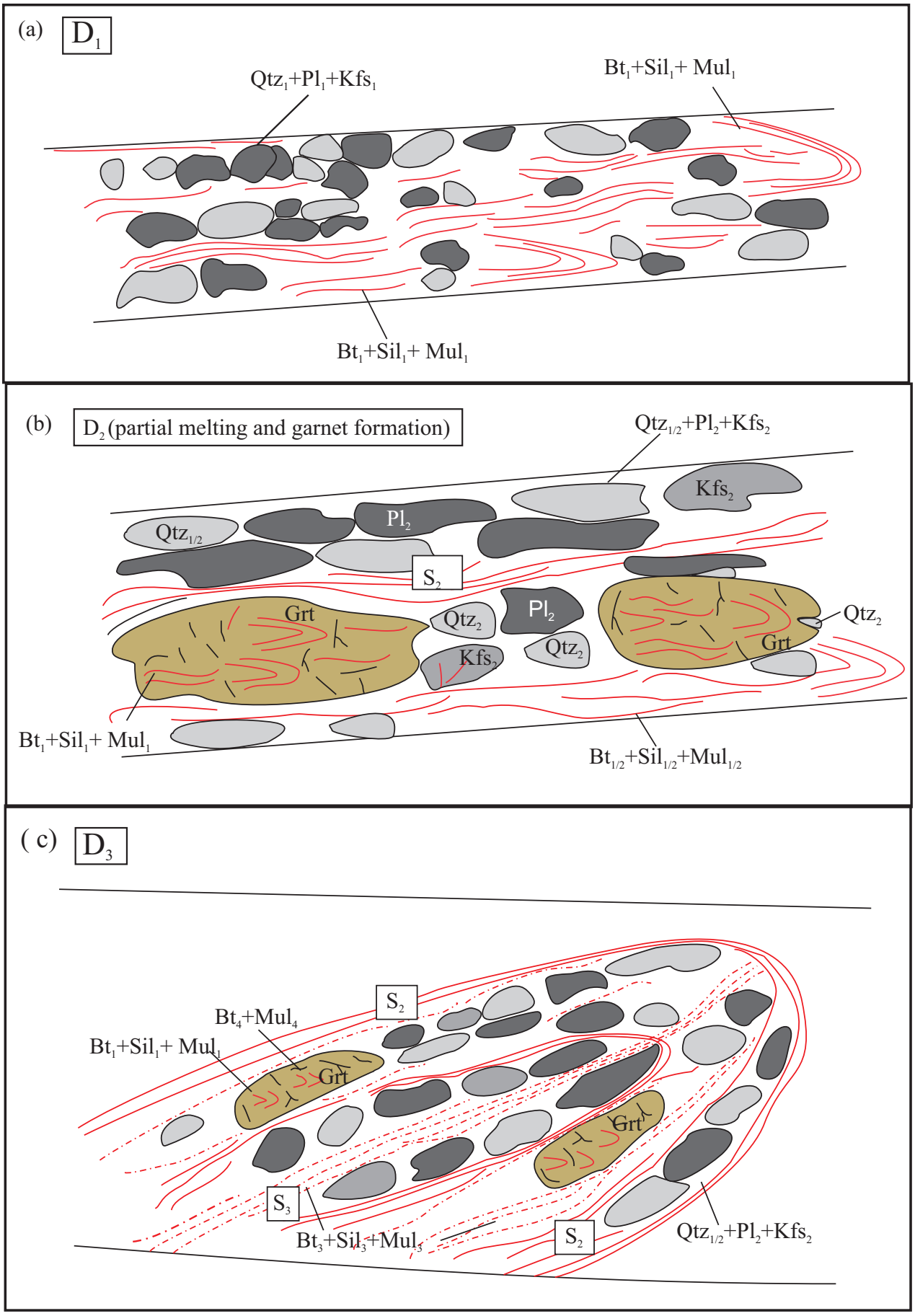

Figure 4

Figure 5 A-D

Click here to download Figure Figures 5a-d.eps

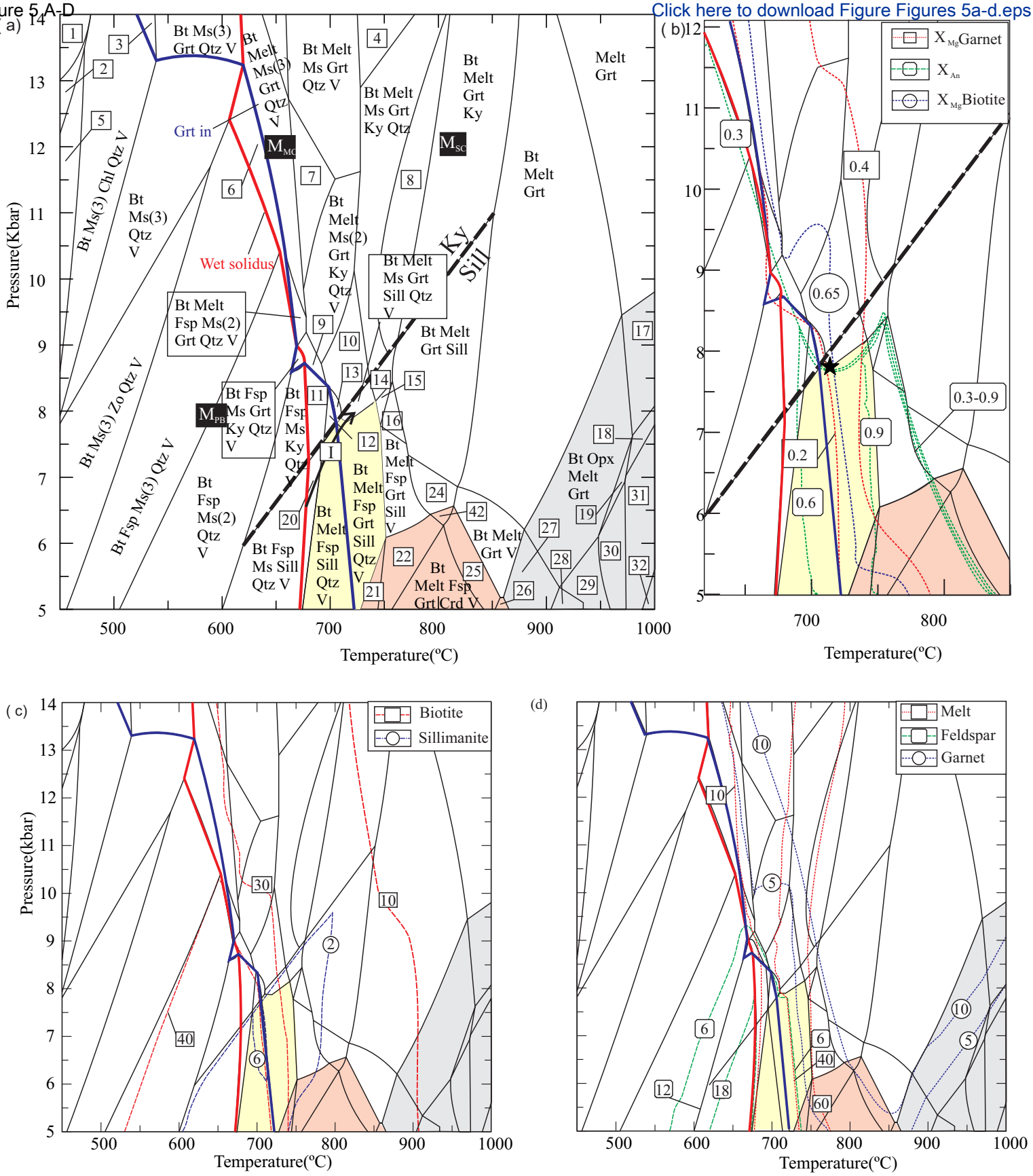

1: Bt Ms(2) Ctd Law Chl Qtz V	2: Bt Ms(2) Law Chl Qtz V	3: Bt Ms(3) Grt Chl Qtz V	4: Bt Melt Ms Grt Qtz
5: Bt Ms(3) Zo Chl Qtz V	6: Bt Melt Ms(3) Qtz V	7: Bt Melt Ms(2) Grt Qtz V	8: Bt Melt Grt Ky Qtz
9: Bt Melt Fsp Ms Grt Ky Qtz V	10: Bt Melt Ms Grt Ky Qtz V	11: Bt Melt Fsp Ms Ky Qtz V	12: Bt Melt Fsp Ky Qtz V
13: Bt Melt Fsp Grt Ky Qtz V	14: Bt Melt Ms Grt Sill Qtz	15: Bt Melt Fsp Grt Sill Qtz	16: Bt Melt Fsp Grt Sill
17: Opx Melt Grt	18: Opx Melt Grt Spr	19: Bt Opx Melt Grt Spr	20: Bt Melt Fsp Ms Sill Qtz V
21: Bt Melt Fsp Grt Sill Crd Qtz V	22: Bt Melt Fsp Grt Sill Crd V	23: Bt Melt Grt Sill Crd V	24: Bt Melt Grt Sill V
25: Bt Melt Grt Crd V	26: Bt Opx Melt Grt Crd V	27: Bt Opx Melt Grt V	28: Bt Opx Melt V
29: Bt Opx Melt	30: Bt Opx Melt Spr	31: Opx Melt Spr	32: Opx Melt

Figure 5

Figure 5 E-F

Click here to download Figure Figures 5e-f.eps

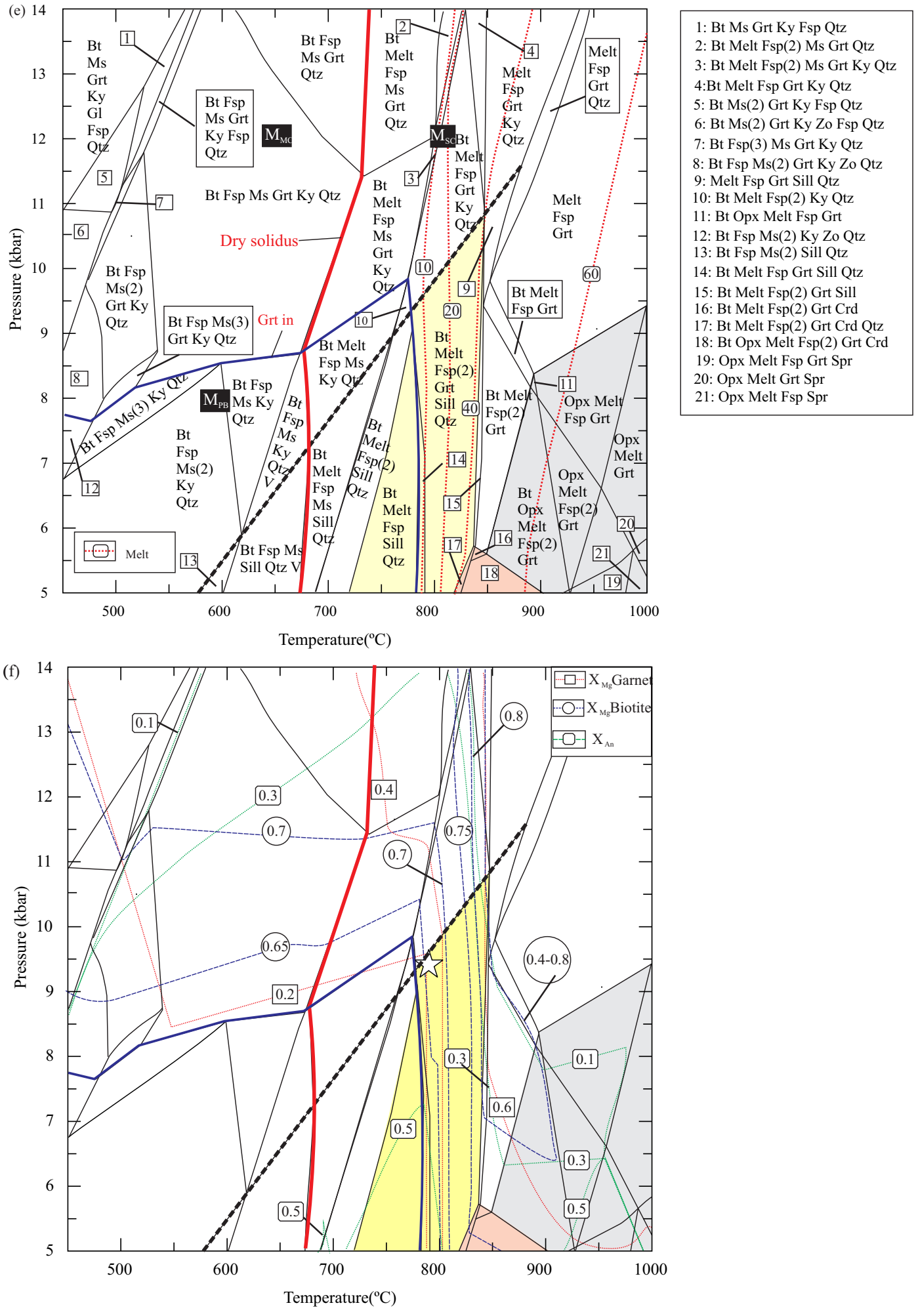

Figure 5

Figure 6

Click here to download Figure Figure 6.eps

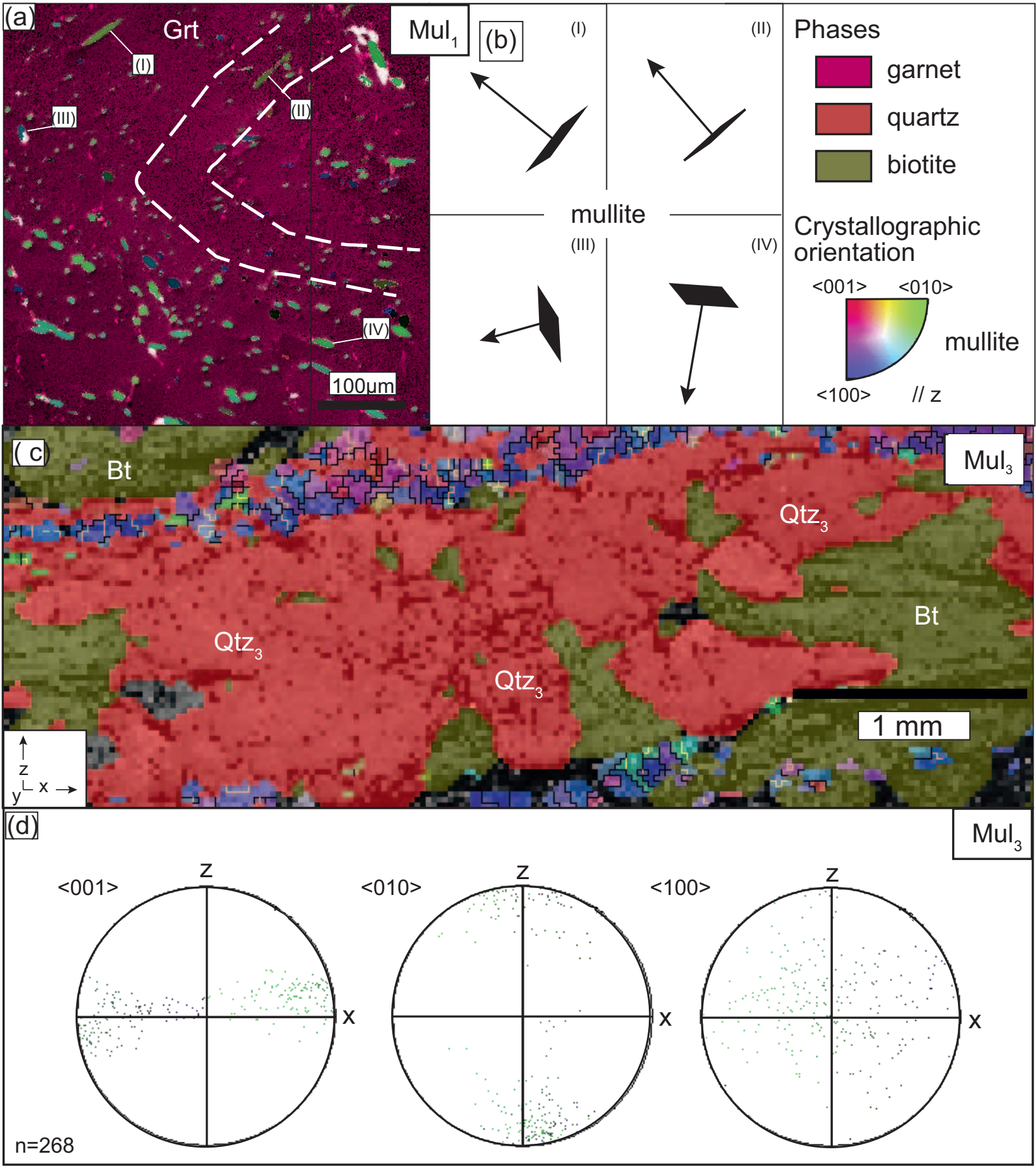

Figure 7

Click here to download Figure figure7.eps

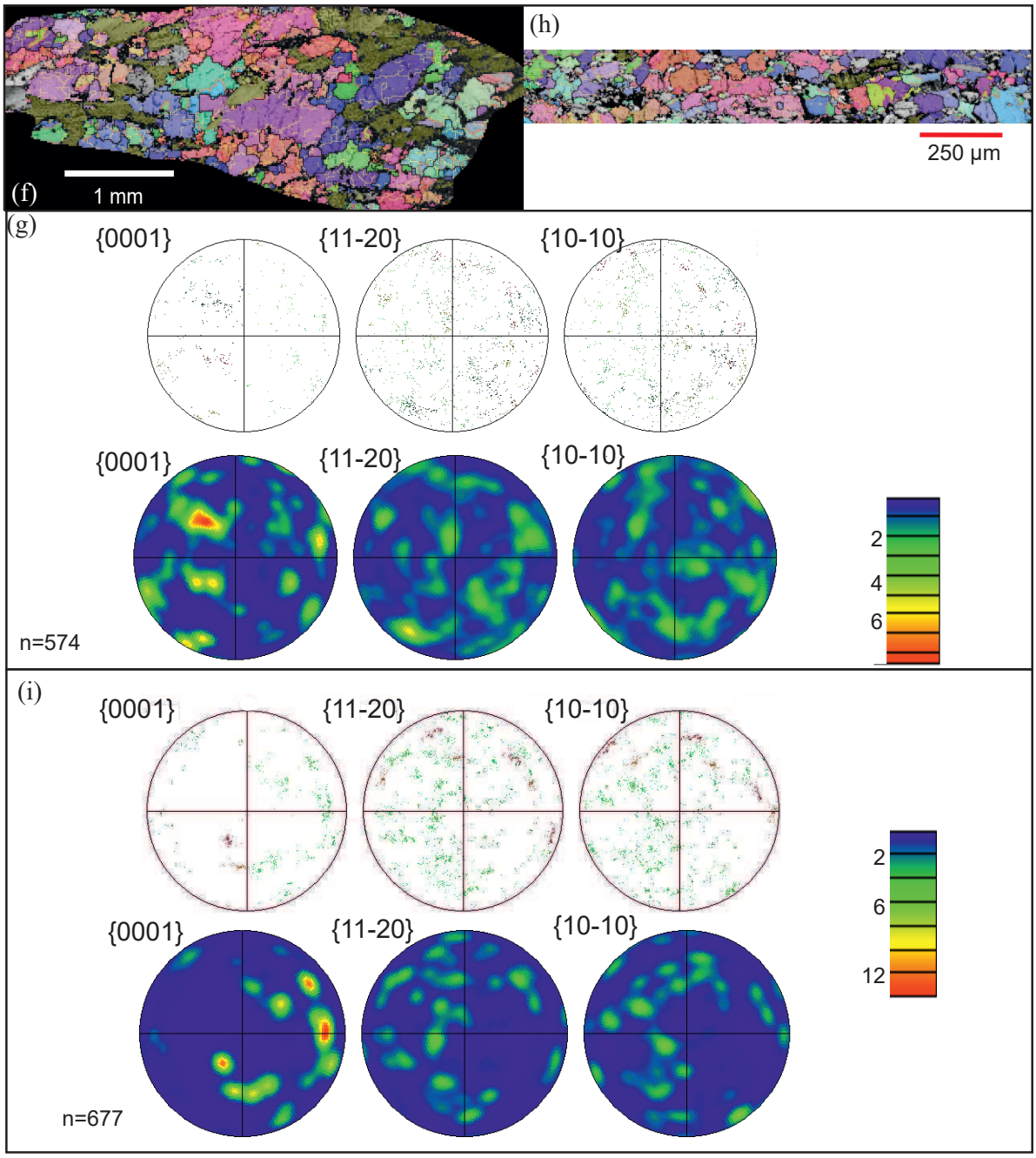

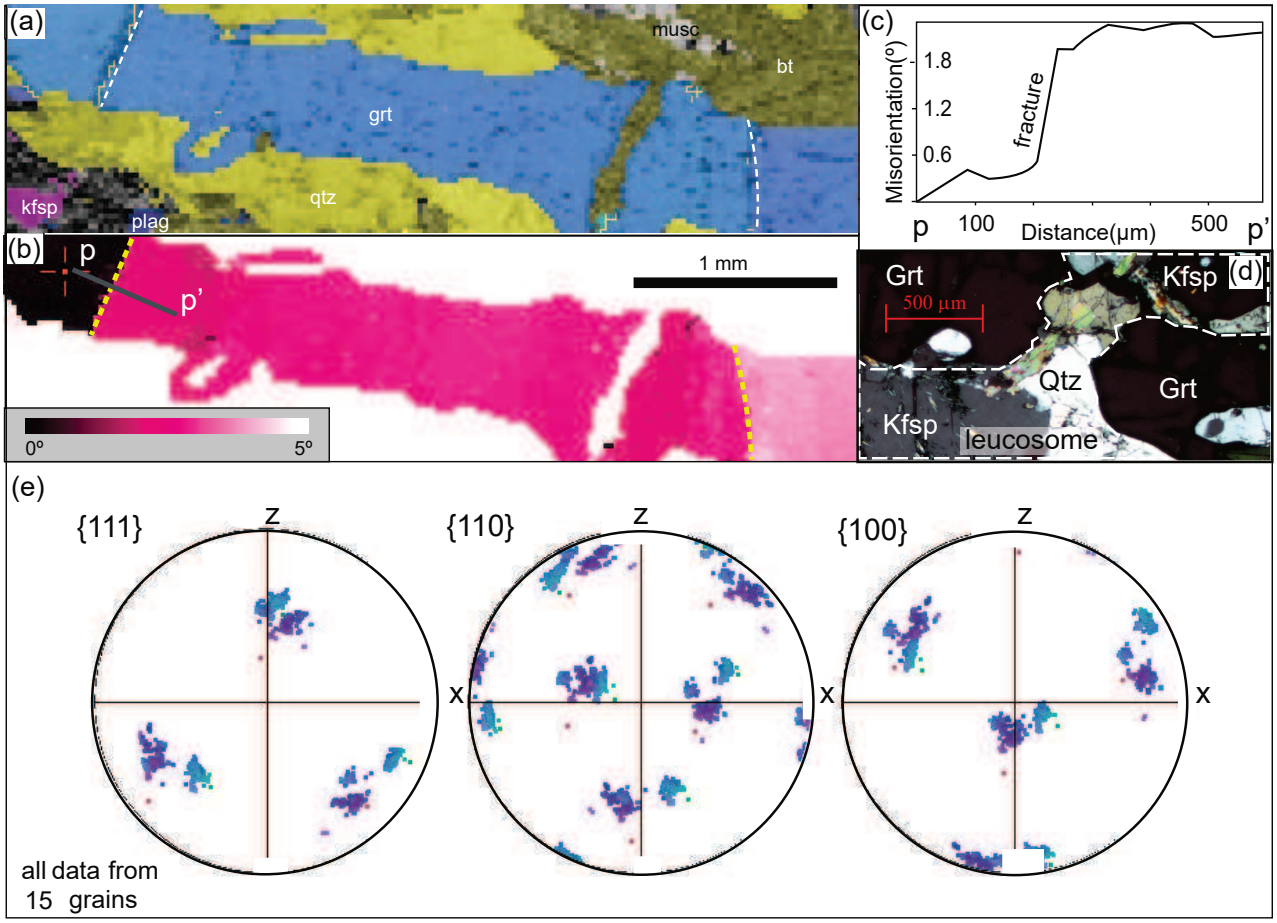

Figure 8

Figure 9

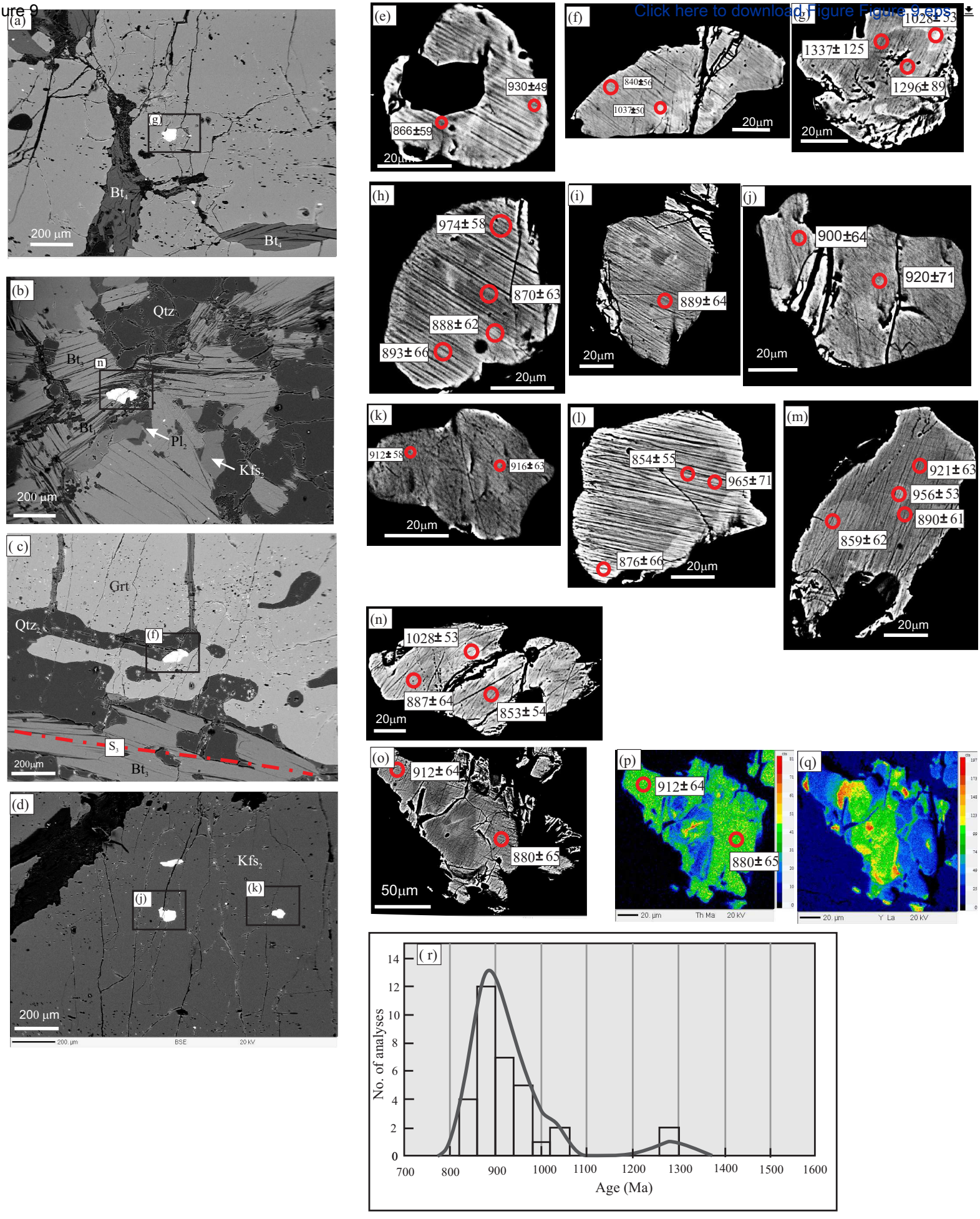

Figure 9

Figure 10

Click here to download Figure Figure 10.eps

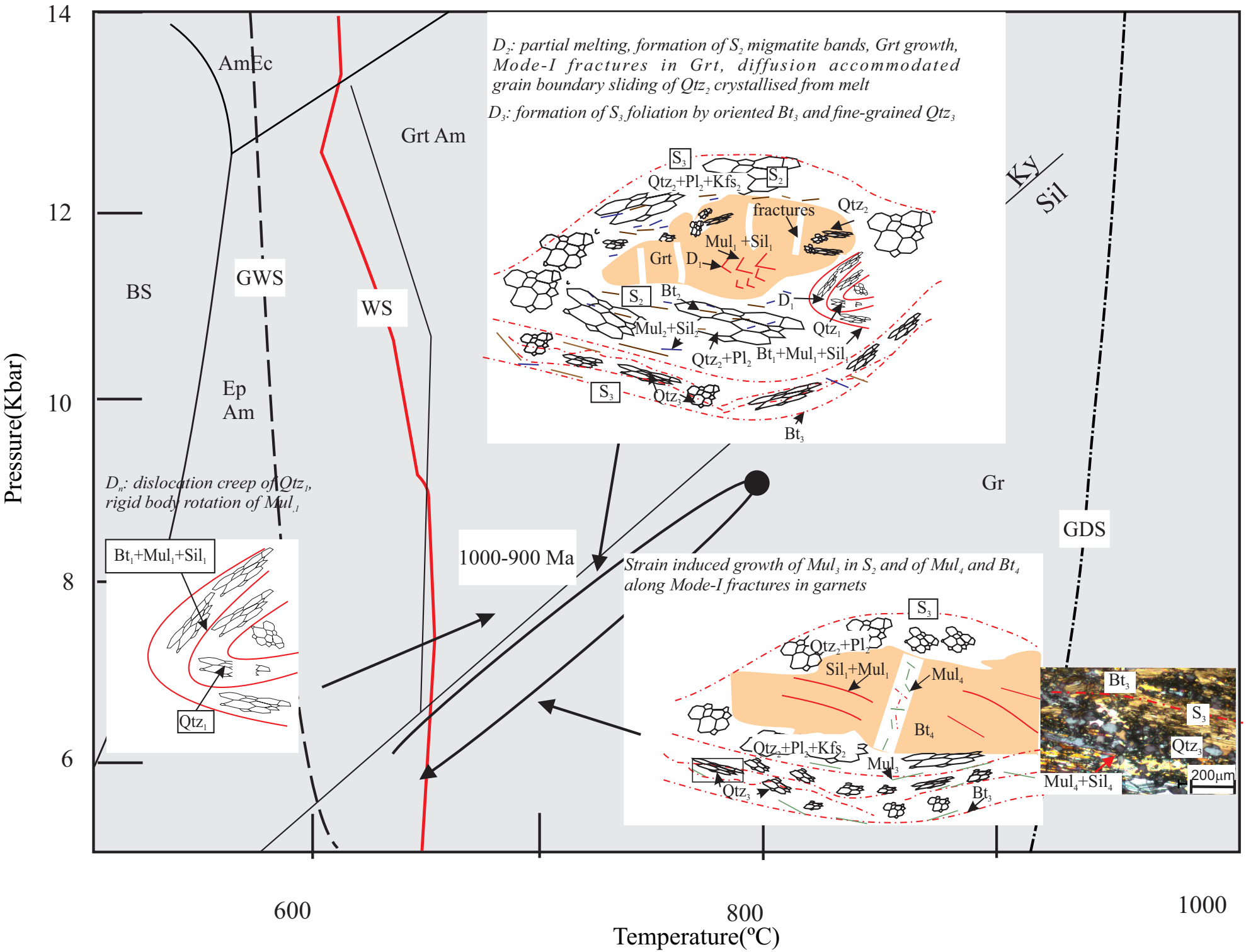

Figure 10

Table 1: Characteristics of microstructures and mineral assemblages

Microstructure type (S = foliation, L – lineation, F-fold, D-deformation)	Mineral assemblage	Main features	Metamorphic reactions leading to assemblage and P-T conditions	Inferred deformation mechanism(s)	Additional Comments
D_1	Mul_1, Sil_1, Qtz_1, Bt_1	Mul_1 grains forming two limbs of the crenulations included in garnet porphyroblast show contrasting orientations (Figs 3a; 6a-b). Rootless fold hinge (Figs 3a, 7a). Qtz_1 shows strong CPO (Figs 7b-c).	~ 650-700^{0}C	Strong CPO indicates activity of prism <c> slip with solid state dislocation creep.	High strain persisted before partial melting and formation of gneissic band S_2.
D_2; S_2	Grt, Qtz_2, Kfs_2, Pl_2, Bt_2, Mul_2	Qtz_2 and Kfs_2 present in the pressure shadows of garnet and within the interfolial domains of S_3. Inclusions of rounded Qtz_1 grain in Kfs_2, bulbous and lobate Qtz_2 grains intergrown with garnet. Mode I fractures filled with Bt_4, Mul_4 are observed in garnet porphyroblasts.(Fig. 3a, d) Absence of subgrain boundaries in garnet. (Fig. 8 a, c) Qtz_2 grains show weak CPOs (Figs 7 d-g).	$Bt_1 + Sil_1 + Qtz_1 + Pl_1 + H_2O \rightarrow$ garnet + melt (crystallized to form Qtz_2, $Kfsp_2$) ~ 725°C and ~ 8 kbar	Weak CPOs of Qtz_2 resulted due tocrystallization from the melt. No crystal plastic deformation is noted in garnet. Mode I fracturesin garnet interpreted to be formed due to high fluidpressure and differential pure shear stresses.	Elongated nature of garnet grains is not due to crystal plastic deformation but rather garnet porphyroblasts have replaced pre-existing foliation of Bt_1, Sil_1, Mul_1 and Qtz_1. Weak CPOs of Qtz_2 and fractures in Grt indicate melt present deformation.
S_3	Bt_3, Sil_3, Mul_3, Qtz_2, Qtz_3	Foliation (Qtz_3, Bt_3, Mul_3) warps around garnet porphyroblast and leucosome domains ,Fig. 3a) Fine-grained Qtz_3 interleaved with Bt_{3b}, Mul_{3b} show weak CPO (Figs 7h-i). Mul_{3b} shows strong CPO (Figs 6c-d).	≥500°C	Strong CPO of Mul_{3b} and weak CPO of Qtz_3 (fine-grained) indicate solid state deformation in former restitic areas.	High-strain that prevailed post-anatexis was accommodated by the fine-grained polygonal (prograde) Qtz_3 by diffusion creep.

Table 2

Table 2: Representative mineral chemical analyses (EPMA) from RAM-1

	Grain 1		Grain 2					Grain 3			
Min	Grt	Grt	Grt	Grt	Grt	Grt	Grt	Grt	Grt	Grt	Grt
	C	R^Bt$_3$	R^Qtz$_2$	C	R^Bt$_4$	C	C	R^Qtz$_2$	C	C	C
SiO_2	38.17	37.87	38.2	38.15	37.68	38.19	38.32	38.12	38.31	38.2	38.2
TiO_2	0.02	0.03	0.11	0	0.02	0	0.01	0	0.03	0	0.05
Al_2O_3	20.98	21.12	20.97	20.7	20.5	21.06	20.9	20.93	20.92	21.16	20.82
Cr_2O_3	0	0.01	0	0.02	0.04	0.03	0.01	0	0	0	0.01
Fe_2O_3	0	0	0	0	0.45	0	0	1.26	0.45	0.92	0.6
FeO	34.95	35.71	34.17	33.89	36.15	34.69	34.6	33.54	34.4	34.09	34.82
MnO	0.51	0.5	0.38	0.38	0.45	0.51	0.46	0.33	0.36	0.41	0.46
MgO	4.48	4.03	4.81	4.77	3.66	4.71	4.53	5.35	5.09	5.14	4.8
CaO	1.37	1.39	1.41	1.4	1.4	1.36	1.34	1.41	1.43	1.39	1.47
Na_2O	0.05	0.02	0.03	0.06	0.02	0.06	0.02	0.06	0.03	0.05	0
K_2O	0	0	0	0.01	0.02	0	0	0.03	0.01	0	0
Totals	100.53	100.68	100.08	99.38	100.38	100.61	100.19	101.03	101.02	101.36	101.23
Oxygens	12	12	12	12	12	12	12	12	12	12	12
Si	3.027	3.011	3.031	3.047	3.019	3.022	3.042	2.998	3.017	2.998	3.011
Ti	0.001	0.002	0.007	0	0.001	0	0.001	0	0.002	0	0.003
Al	1.961	1.979	1.961	1.949	1.936	1.965	1.956	1.941	1.942	1.958	1.935
Cr	0	0.001	0	0.001	0.003	0.002	0.001	0	0	0	0.001
Fe^{3+}	0	0	0	0	0.027	0	0	0.075	0.026	0.055	0.036
Fe^{2+}	2.318	2.374	2.267	2.263	2.422	2.296	2.297	2.206	2.265	2.237	2.296
Mn	0.034	0.034	0.026	0.026	0.031	0.034	0.031	0.022	0.024	0.027	0.031
Mg	0.529	0.477	0.569	0.568	0.437	0.555	0.536	0.627	0.597	0.601	0.564
Ca	0.116	0.118	0.12	0.12	0.12	0.115	0.114	0.119	0.121	0.117	0.124
Na	0.008	0.003	0.005	0.009	0.003	0.009	0.003	0.009	0.005	0.008	0
K	0	0	0	0.001	0.002	0	0	0.003	0.001	0	0
Sum	7.995	7.999	7.984	7.984	8	7.999	7.981	8	8	8	8
X_{Alm}	0.77	0.79	0.76	0.76	0.80	0.77	0.77	0.74	0.75	0.75	0.76
X_{Prp}	0.18	0.16	0.19	0.19	0.15	0.19	0.18	0.21	0.20	0.20	0.19
X_{Grs}	0.04	0.04	0.04	0.04	0.04	0.04	0.04	0.04	0.04	0.04	0.04
X_{Sps}	0.01	0.01	0.01	0.01	0.01	0.01	0.01	0.01	0.01	0.01	0.01
X_{Mg}	0.19	0.17	0.20	0.20	0.15	0.19	0.19	0.22	0.21	0.21	0.20

Table 2 (continued)

	Grain 3				Grain 4						
Min	Grt	Grt	Grt	Grt	Grt	Grt	Grt	Grt	Grt	Bt_1	Bt_2
	R^Qtz_2	R^Qtz_2	C	R^Qtz_2	R^Bt_2	C	C	C	C	I^Grt	M(C)
SiO_2	38.12	38.18	38.17	38.2	37.47	37.69	37.99	37.44	37.68	35.85	35.98
TiO_2	0	0	0	0	0	0	0	0.02	0	2.11	1.91
Al_2O_3	20.43	20.79	20.48	21.06	20.86	20.7	21	20.83	20.74	17.67	17.77
Cr_2O_3	0.01	0.04	0.05	0.03	0.06	0.08	0.08	0.1	0	0.01	0.06
Fe_2O_3	0.67	0.45	1.22	0.3	0.16	0	0.06	0.73	1.19	0	0
FeO	35.5	36.06	35.46	35.7	32.6	32.67	32.87	32.3	32.06	16.87	17.2
MnO	0.44	0.47	0.47	0.36	0.37	0.31	0.37	0.32	0.42	0.08	0
MgO	4.41	4.29	4.49	4.43	5.57	5.62	5.77	5.78	5.83	11.28	11.7
CaO	1.34	1.15	1.29	1.34	1.39	1.49	1.48	1.45	1.52	0.02	0.03
Na_2O	0	0	0.01	0	0.02	0	0	0	0.05	0.09	0.18
K_2O	0.02	0	0	0	0.01	0.02	0	0	0	9.58	9.38
Totals	100.94	101.42	101.64	101.42	98.51	98.58	99.62	98.97	99.49	93.56	94.21
Oxygens	12	12	12	12	12	12	12	12	12	11	11
Si	3.025	3.017	3.011	3.012	3.008	3.022	3.014	2.992	2.996	2.751	2.742
Ti	0	0	0	0	0	0	0	0.001	0	0.122	0.109
Al	1.911	1.937	1.904	1.957	1.974	1.957	1.964	1.963	1.944	1.599	1.597
Cr	0.001	0.002	0.003	0.002	0.004	0.005	0.005	0.006	0	0.001	0.004
Fe^{3+}	0.04	0.027	0.072	0.018	0.009	0	0.003	0.044	0.071	0	0
Fe^{2+}	2.356	2.383	2.339	2.354	2.189	2.191	2.181	2.159	2.132	1.083	1.096
Mn	0.03	0.031	0.031	0.024	0.025	0.021	0.025	0.022	0.028	0.005	0
Mg	0.522	0.505	0.528	0.52	0.666	0.672	0.682	0.688	0.691	1.29	1.329
Ca	0.114	0.097	0.109	0.113	0.12	0.128	0.126	0.124	0.13	0.002	0.002
Na	0	0	0.002	0	0.003	0	0	0	0.008	0.013	0.027
K	0.002	0	0	0	0.001	0.002	0	0	0	0.938	0.912
Sum	8	8	8	8	8	7.998	8	7.999	8	7.804	7.818
X_{Alm}	0.78	0.79	0.78	0.78	0.73	0.73	0.72	0.72	0.72		
X_{Prp}	0.17	0.17	0.18	0.17	0.22	0.22	0.23	0.23	0.23		
X_{Grs}	0.04	0.03	0.04	0.04	0.04	0.04	0.04	0.04	0.04		
X_{Sps}	0.01	0.01	0.01	0.01	0.01	0.01	0.01	0.01	0.01		
X_{Mg}	0.18	0.17	0.18	0.18	0.23	0.23	0.24	0.24	0.24	0.54	0.55

Table 2 (continued)

Min	Bt_2	Bt_2	Bt_2	Bt_3	Bt_3	Bt_3	Bt_3	Bt_3	Bt_3	Bt_3	Bt_3	Bt_3
	M(C)	M(C)	M(C)	M(C)	M(C)	M(C)	M(C)	M(C)	M(C)	M^Grt Rim	M^Grt Rim	M^Grt Rim
SiO_2	35.64	35.68	35.57	36.7	36.3	34.72	35.81	36.53	36.37	36.74	36.36	36.32
TiO_2	1.87	1.99	1.74	1.88	1.21	1.24	1.18	1.94	2.13	2.21	2	2.13
Al_2O_3	17.93	17.71	17.18	17.55	18.38	18.37	18.51	17.84	18.08	18.62	18.86	18.88
Cr_2O_3	0.03	0.03	0.05	0.1	0	0.08	0	0.03	0	0.07	0.06	0.1
Fe_2O_3	0	0	0	0	0	0	0	0	0	0	0	0
FeO	16.38	16.58	16.53	17.07	16.3	16.35	16.74	17	17.28	16.62	16.87	16.1
MnO	0.04	0.03	0.07	0.03	0.02	0	0	0.04	0	0	0	0.03
MgO	11.73	11.71	11.67	11.93	12.4	11.61	12.15	12.02	11.76	12.1	11.78	11.97
CaO	0.12	0.19	0.02	0.11	0.04	0.22	0.03	0.05	0	0.04	0.02	0.03
Na_2O	0.13	0.11	0.11	0.14	0.17	0.45	0.16	0.19	0.17	0.25	0.16	0.18
K_2O	9.48	9.06	9.52	9.36	9.6	9.26	9.49	9.31	9.53	9.39	9.28	9.23
Totals	93.35	93.09	92.46	94.87	94.42	92.3	94.07	94.95	95.32	96.04	95.39	94.97
Oxygens	11	11	11	11	11	11	11	11	11	11	11	11
Si	2.735	2.742	2.762	2.771	2.747	2.7	2.726	2.754	2.738	2.73	2.722	2.722
Ti	0.108	0.115	0.102	0.107	0.069	0.073	0.068	0.11	0.121	0.124	0.113	0.12
Al	1.622	1.604	1.573	1.562	1.639	1.684	1.661	1.586	1.604	1.631	1.665	1.668
Cr	0.002	0.002	0.003	0.006	0	0.005	0	0.002	0	0.004	0.004	0.006
Fe^{3+}	0	0	0	0	0	0	0	0	0	0	0	0
Fe^{2+}	1.051	1.066	1.073	1.078	1.031	1.063	1.066	1.072	1.088	1.033	1.056	1.009
Mn	0.003	0.002	0.005	0.002	0.001	0	0	0.003	0	0	0	0.002
Mg	1.341	1.341	1.35	1.342	1.398	1.346	1.379	1.351	1.319	1.34	1.315	1.337
Ca	0.01	0.016	0.002	0.009	0.003	0.018	0.002	0.004	0	0.003	0.002	0.002
Na	0.019	0.016	0.017	0.02	0.025	0.068	0.024	0.028	0.025	0.036	0.023	0.026
K	0.928	0.888	0.943	0.902	0.927	0.919	0.922	0.895	0.915	0.89	0.886	0.883
Sum	7.82	7.793	7.829	7.8	7.841	7.877	7.848	7.804	7.81	7.792	7.786	7.776
X_{Mg}	0.56	0.56	0.56	0.55	0.58	0.56	0.56	0.56	0.55	0.56	0.55	0.57

C: Core, R: Rim, I: Inclusion; M: Matrix,^: against.

Table 2 (continued)

Min	Bt_4	Bt_4	Kfs_2	Kfs_2	Kfs_2	Pl_2	Pl_2	Pl_2	Pl_2	Pl_2
	^Grt fracture	^Grt fracture	M(C)	M(C)	M(C)	M(C)	M(C)	M(C)	M(C)	M(C)
SiO_2	36.35	35.87	63.53	63.86	63.96	60.83	61.46	60.76	61.03	60.84
TiO_2	0.1	0.59	0.04	0.06	0.07	0.02	0	0.02	0.01	0.06
Al_2O_3	18.93	19.57	17.27	17.59	17.79	23.29	23.34	23.12	23.43	23.21
Cr_2O_3	0.03	0.01	0.04	0	0.04	0.04	0	0	0	0.03
Fe_2O_3	0.91	0.86	0.18	0	0	0.03	0.04	0.06	0.11	0.01
FeO	12.63	14.1	0	0	0	0	0	0	0	0
MnO	0	0	0	0	0	0	0	0	0	0.07
MgO	14.35	13.42	0	0.01	0	0	0	0	0	0.02
CaO	0.04	0.08	0.06	0	0.02	5.82	5.75	5.82	5.93	5.94
Na_2O	0.16	0.61	1.98	1.79	1.58	8.25	8.23	8.44	8.32	8.21
K_2O	9.67	8.96	13.69	13.37	13.69	0.19	0.3	0.17	0.18	0.2
Totals	93.17	94.08	96.79	96.68	97.15	98.47	99.12	98.39	99.01	98.59
Oxygens	11	11	8	8	8	8	8	8	8	8
Si	2.744	2.695	3.014	3.019	3.013	2.744	2.753	2.746	2.74	2.744
Ti	0.006	0.033	0.001	0.002	0.002	0.001	0	0.001	0	0.002
Al	1.685	1.733	0.966	0.981	0.988	1.239	1.233	1.232	1.24	1.234
Cr	0.002	0.001	0.002	0	0.001	0.001	0	0	0	0.001
Fe^{3+}	0.053	0.049	0.006	0	0	0.001	0.001	0.002	0.004	0
Fe^{2+}	0.797	0.886	0	0	0	0	0	0	0	0
Mn	0	0	0	0	0	0	0	0	0	0.003
Mg	1.614	1.503	0	0.001	0	0	0	0	0	0.001
Ca	0.003	0.006	0.003	0	0.001	0.281	0.276	0.282	0.285	0.287
Na	0.023	0.089	0.182	0.164	0.144	0.722	0.715	0.74	0.724	0.718
K	0.931	0.859	0.829	0.807	0.823	0.011	0.017	0.01	0.01	0.012
Sum	7.859	7.855	5.004	4.974	4.974	5.001	4.996	5.011	5.005	5.001
X_{Mg}	0.67	0.63								
X_{An}						0.28	0.27	0.27	0.28	0.28

C: Core, R: Rim, M: Matrix,^: against; mineral abbreviations are after Kretz (1983).

Table 3: Results of geothermometry

S. No.	Grt	Bt	Bh(°C)	Dg (°C)	FS(°C)	H (°C)	HP(°C)	Average Grt-Bt (°C)
At 8 kbar reference pressure								
1	C	Bt_1^Grt	630	597	731	708	794	692
2	C	Bt_2 (C)	631	640	706	699	763	688
3	C	Bt_2 (C)	628	632	697	693	760	682
4	C	Bt_2 (C)	626	632	688	692	746	677
5	R ^ Qtz (M)	Bt_2 (C)	617	612	671	680	754	667
At 6 kbar reference pressure								
6	R^Bt_4	Bt_4	531	518	515	596	517	535
7	R^Bt_3	Bt_3 (C)	561	518	564	619	615	576
8	R^Bt_3	Bt_3(R^Grt)	556	508	557	609	588	564
9	R^Bt_3	Bt_3 (C)	547	491	536	597	567	548
10	R^Bt_3	Bt_3 (C)	570	530	577	620	615	583
11	R^Bt_3	Bt_3 (C)	563	525	563	613	603	574

Bh: Bhattacharya et al. (1992); Dg: Dasgupta et al. (1991); FS: Ferry and Spear (1978); H: Holdway (2000); HP: Holland and Powell (1998); M: Matrix; I: Inclusion; C: core; R: Rim.

Table 4: XRF data of RAM-1

SiO_2	55.550
Al_2O_3	18.780
Fe_2O_3	8.860
MnO	0.030
MgO	6.520
CaO	1.250
Na_2O	1.360
K_2O	5.240
TiO_2	0.880
P_2O_5	0.070
LOI	1.387
Sum	99.927

Table 5

Table 5: Analytical data (EPMA) for the dated monazites of sample RAM-1

	Texture	Pb	Th	U	Age (Ma)	2 sigma	%error
1	Contact of Qtz_2 in S_2	0.54	10.01	0.83	930	49	5.27
2	Contact of Qtz_2 in S_2	0.36	4.8	1.31	866	59	6.81
3	Contact of garnet and Qtz_2 in S_2	0.37	4.77	1.46	840	56	6.67
4	Contact of garnet and Qtz_2 in S_2	0.62	10.28	0.82	1037	50	4.82
5	Contact of Qtz_3 in S_3	0.33	4.76	1.11	870	63	7.24
6	Contact of Qtz_3 in S_3	0.44	6.89	0.93	974	58	5.95
7	Contact of Qtz_3 in S_3	0.32	5.12	0.82	893	66	7.39
8	Contact of Qtz_3 in S_3	0.35	5.28	1	888	62	6.98
9	Inclusion in Kfs_2 in S_2	0.31	5.43	0.58	920	71	7.72
10	Inclusion in Kfs_2 in S_2	0.34	5.12	0.98	900	64	7.11
11	Inclusion in Kfs_2 in S_2	0.36	6	0.75	916	63	6.88
12	Inclusion in Kfs_2 in S_2	0.4	5.02	1.36	912	58	6.36
13	Overgrowing Bt_3 in S_3	0.33	5.41	0.85	889	64	7.20
14	Contact of Qtz_3 in S_3	0.31	4.83	0.62	991	76	7.67
15	Contact of Qtz_3 in S_3	0.33	4.67	0.84	965	71	7.36
16	Contact of Qtz_3 in S_3	0.31	5.11	0.81	876	66	7.53
17	Contact of Qtz_3 in S_3	0.39	4.95	1.5	854	55	6.44
18	Contact of garnet and Qtz_2 in S_2	0.36	4.62	1.31	867	60	6.92
19	Inclusion in Grt in S_2	0.37	5.84	0.98	896	59	6.58
20	Overgrowing Bt_3 in S_3	0.33	5.26	0.96	859	62	7.22
21	Overgrowing Bt_3 in S_3	0.36	4.31	1.25	921	63	6.84
22	Overgrowing Bt_3 in S_3	0.49	8.07	0.92	956	53	5.54
23	Overgrowing Bt_3 in S_3	0.35	4.57	1.21	890	61	6.85
24	Contact of Qtz_3 in S_3	0.37	4.85	1.34	883	59	6.68
25	Contact of Qtz_2 in S_2	0.31	4.43	0.75	963	74	7.68
26	Overgrowing Bt_3 in S_3	0.33	5.25	0.88	887	64	7.22
27	Overgrowing Bt_3 in S_3	0.55	9.51	0.65	1028	53	5.16
28	Overgrowing Bt_3 in S_3	0.4	4.72	1.66	853	54	6.33
29	Contact of garnet and Qtz_2 in S_2	0.36	3.15	0.84	1273	92	7.23
30	Inclusion in Grt in S_2	0.51	9.34	0.71	954	52	5.45
31	Inclusion in Grt in S_2	0.39	5.05	0.41	1296	89	6.87
32	Contact of Qtz_2 in S_2	0.32	5.2	0.82	880	65	7.39
33	Contact of Qtz_2 in S_2	0.35	5.26	0.92	912	64	7.02

(a)

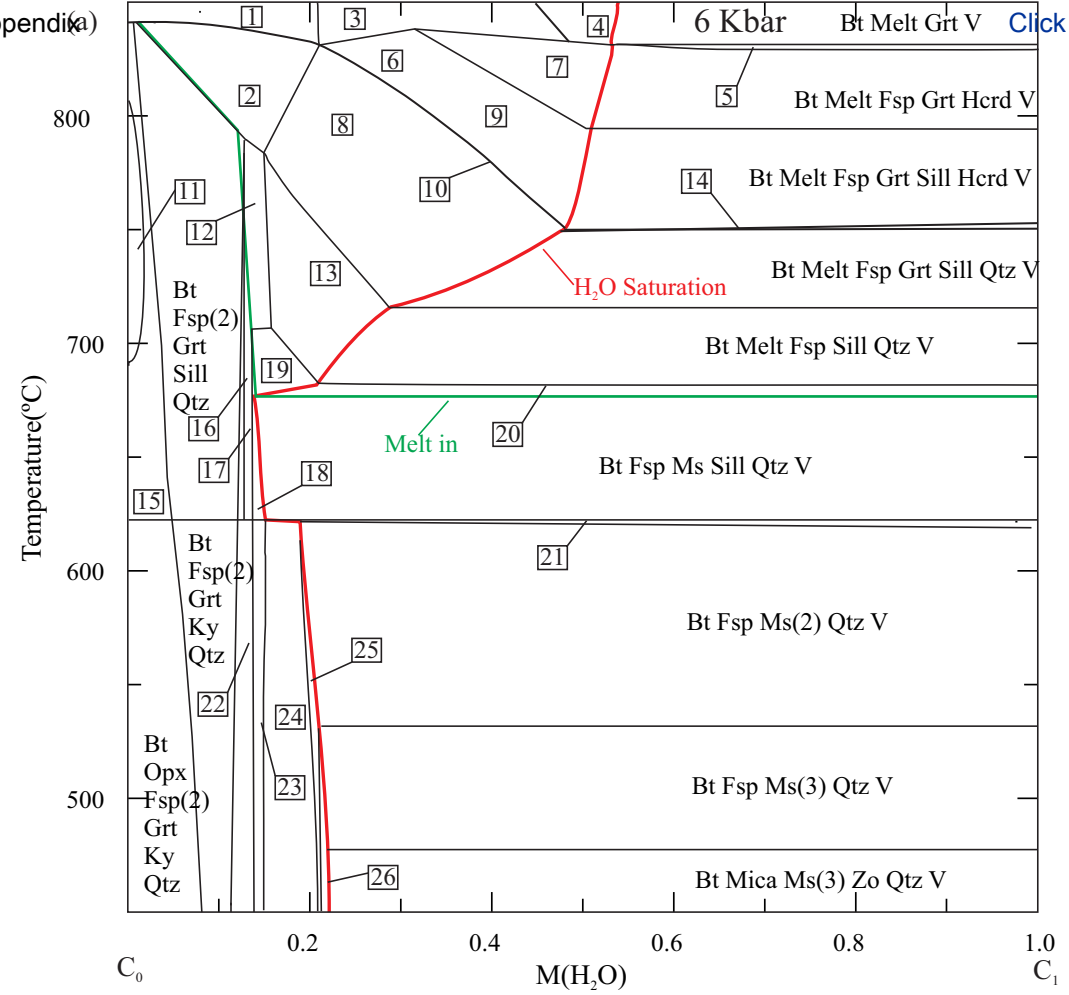

1: Bt Melt Fsp(2) Grt
2: Bt Melt Fsp(2) Grt Sill Qtz
3: Bt Melt Fsp Grt
4: Bio Melt Gt
5: Bt Melt Grt Hcrd V
6: Bt Melt Fsp Grt Sill
7: Bt Melt Fsp Grt Hcrd
8: Bt Melt Fsp Grt Sill Qtz
9: Bt Melt Fsp Grt Sill Hcrd
10: Bt Melt Fsp Grt Sill Hcrd Qtz
11: Bt Opx Fsp(2) Grt Osm Sill Qtz
12: Bt Melt Fsp(2) Sill Qtz
13: Bt Melt Fsp Sill Qtz
14: Bt Melt Fsp Grt Sill Hcrd Qtz V
15: Bt Opx Fsp(2) Grt Sill Qtz
16: Bio Fsp(2) Sill Qtz
17: Bt Fsp(2) Ms Sill Qtz
18: Bt Fsp Ms Sill Qtz
19: Bt Melt Fsp Ms Sill Qtz
20: Bt Melt Fsp Ms Sill Qtz V
21: Bt Fsp Ms(2) Ky Qtz V
22: Bt Fsp(2) Ms Ky Qtz
23: Bt Fsp Ms Ky Qtz
24: Bt Fsp Ms(2) Ky Qtz
25: Bt Fsp Ms(2) Qtz
26: Bt Fsp Ms(3) Qtz

(b)

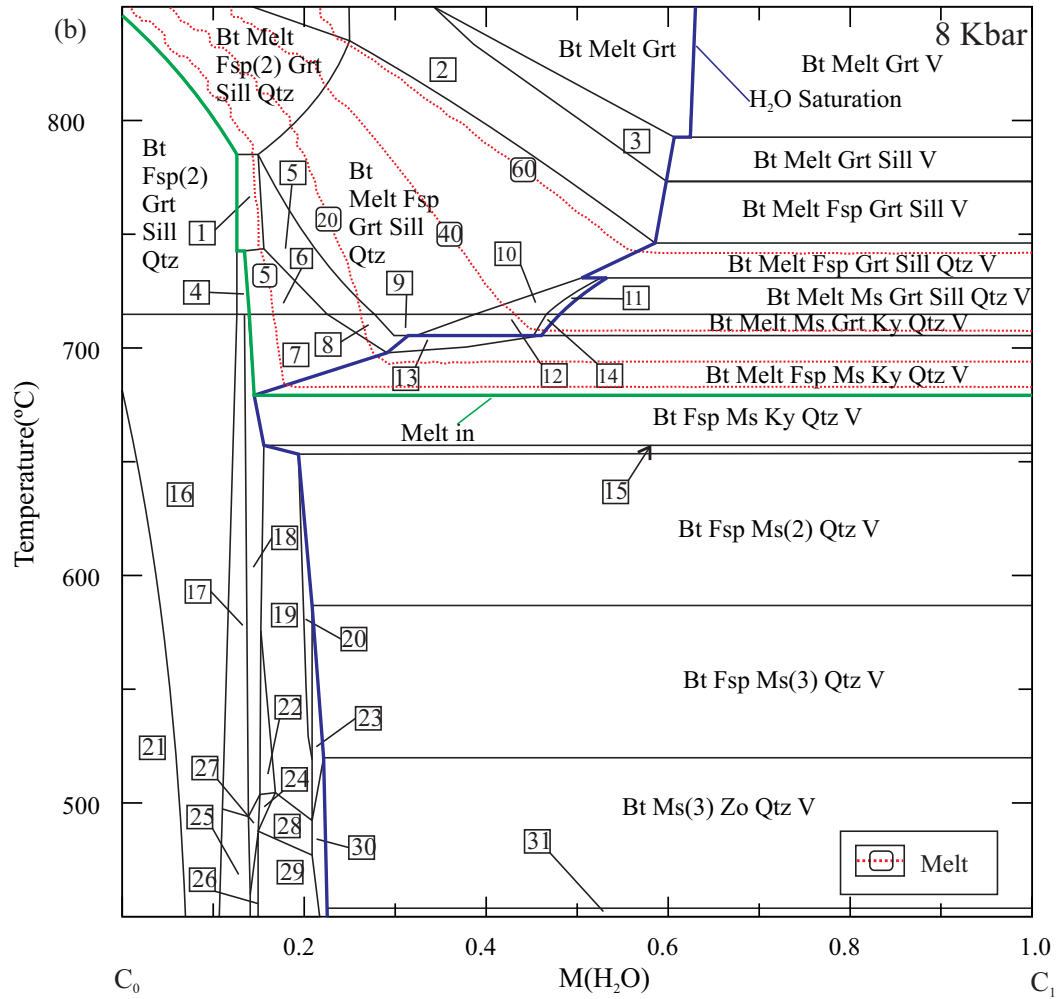

1: Bt Melt Fsp(2) Sill Qtz
2: Bt Melt Fsp Grt Sill
3: Bt Melt Grt Sill
4: Bt Fsp(2) Ms Sill Qtz
5: Bt Melt Fsp Sill Qtz
6: Bt Melt Fsp Ms Sill Qtz
7: Bt Melt Fsp Ms Ky Qtz
8: Bt Melt Fsp Ky Qtz
9: Bt Melt Fsp Grt Ky Qtz
10: Bt Melt Fsp Ms Grt Sill Qtz
11: Bt Melt Ms Grt Sill Qtz
12: Bt Melt Fsp Ms Grt Ky Qtz
13: Bt Melt Fsp Ky Qtz V
14: Bt Melt Ms Grt Ky Qtz
15: Bt Fsp Ms(2) Ky Qtz V
16: Bt Fsp(2) Grt Ky Qtz
17: Bt Fsp(2) Ms Ky Qtz
18: Bt Fsp Ms Ky Qtz
19: Bt Fsp Ms(2) Ky Qtz
20: Bt Fsp Ms(2) Qtz
21: Bt Opx Fsp(2) Grt Ky Qtz
22: Bt Fsp Ms(3) Ky Qtz
23: Bt Fsp Ms(3) Qtz
24: Bt Fsp Ms(3) Grt Ky Qtz
25: Bt Fsp(2) Ms Grt Ky Qtz
26: Bt Fsp Ms Grt Ky Zo Qtz
27: Bt Fsp Ms Grt Ky Qtz
28: Bt Fsp Ms(2) Grt Ky Qtz
29: Bt Fsp Ms(2) Grt Ky Zo Qtz
30: Bt Ms(2) Zo Qtz
31: Bt Ms(3) Qtz V